IEEE Access
Multidisciplinary | Rapid Review | Open Access Journal

Received July 8, 2020, accepted July 16, 2020, date of publication July 21, 2020, date of current version July 30, 2020.

Digital Object Identifier 10.1109/ACCESS.2020.3010889

Performance Analysis of Non-Ideal Sectorized SFR Cellular Systems in Rician Fading Channels With Unbalanced Diversity

HENRY CARVAJAL [1], (Member, IEEE), NATHALY OROZCO [1], DANIEL ALTAMIRANO [2,3], (Student Member, IEEE), AND CELSO DE ALMEIDA [3]

[1]Faculty of Engineering and Applied Sciences (FICA), Telecommunications Engineering, Universidad de Las Américas (UDLA), Quito 170125, Ecuador
[2]Electrical and Electronics Department (DEEL), Universidad de las Fuerzas Armadas-ESPE, Sangolquí 171103, Ecuador
[3]School of Electrical and Computer Engineering, University of Campinas (UNICAMP), Campinas 13083-852, Brazil

Corresponding author: Henry Carvajal (henry.carvajal@udla.edu.ec)

This work was supported by the Universidad de Las Américas (UDLA), Quito, Ecuador under Project ERT.HCM.19.02.

ABSTRACT Nowadays, low reuse factors are used in cellular systems because of high traffic demand, despite it produces high co-cell interference (CCI) levels. Consequently, soft-frequency-reuse (SFR) and sectorization are used to improve the spectral efficiency and to mitigate CCI. In addition, diversity techniques are necessary for a good system performance. Motivated by this scenario, for the uplink of orthogonal-frequency-division multiple access (OFDMA) systems, the bit error rate (BER) and the cellular spectral efficiency using multilevel-quadrature-amplitude-modulation (M-QAM) and maximal-ratio-combining (MRC) in Rician fading channels are analyzed, where diversity branches have different Rician $\mathcal{K}$-factors (unbalanced diversity). SFR is used assuming non-ideal sectorized cells due to the irregular radiation pattern of base station antennas. An exact integral-form expression and a closed-form upper-bound to evaluate the BER are obtained. In addition, an algorithm, and an expression to calculate the cellular spectral efficiency are presented considering that a target BER must be guaranteed for all users in the cell. From the analysis, it is determined that the BER can be reduced and the spectral efficiency can be improved if some system operating parameters are selected in an adequate manner. Thus, it was noticed that the number of diversity branches, the sum of the $\mathcal{K}$ factors of these branches, and the antenna type, are decisive to guarantee the target BER and to maximize the cellular spectral efficiency.

INDEX TERMS Bit error rate, interference, soft-frequency-reuse, non-ideal sectorization, diversity.

I. INTRODUCTION

Cellular networks are experiencing a crescent increase in traffic demand because a large number of devices connect to them [1]. Hence, a large number of channels must be allocated in each cell. If an increase in bandwidth is not possible, then the channel reuse factor is decreased, that implies higher interference, and therefore, compromises the system performance. On the other hand, fifth-generation (5G) wireless systems aim ultra-reliable-low-latency communications (URLLC), that among some things, implies low bit error rate (BER) for the proper system operation [2].

In wireless systems, the transmitted signals arrive at the receiver via different paths. This phenomenon is modeled as a random channel gain attenuating the signal, whose envelope is known as fading. When one path, typically, a line of sight (LOS) path, is much stronger than the others, the fading amplitude can be characterized by a Rician distribution. One parameter that features Rician fading is the ratio of the power contributions between the stronger path and the remaining multipaths and is named as $\mathcal{K}$ factor [3]. In [4], the BER of orthogonal-frequency-division multiple access (OFDMA) was evaluated for Rician fading via simulations. In [5], a scenario with co-channel interference was analyzed using the Chernoff bound to obtain BER expressions for binary modulations, which are accurate only in the low signal-to-noise-ratio (SNR) region. In particular, co-channel interference is recognized as one of the major factors that limits the capacity and link quality of a wireless communications system [6]. In [7], an approximate expression of the average symbol error

The associate editor coordinating the review of this manuscript and approving it for publication was Mauro Fadda.

rate (SER) for any modulation is determined considering the infinite series representation of the Bessel function. This expression is accurate in the high SNR region.

One widely used technique to improve the wireless systems performance is diversity, where some replicas of the same received signals are obtained so that they are affected by independent fading. The combination method for these replicas that maximizes the SNR is maximal-ratio-combining (MRC) [8]. The standard assumption that all diversity branches have the same power is typically assumed. However, some works consider that unbalanced diversity branches reflect a more realistic and a more general scenario [9]–[11]. For Rician fading, it implies that the diversity branches have different $\mathcal{K}$ factors. Only a few works evaluate the BER in Rician fading considering the above described scenario. In [12], the impact of correlated diversity branches in Rician fading channels was studied. Asymptotes of the BER for binary modulations and the SER for multilevel quadrature-amplitude-modulation (M-QAM) are obtained. The expressions are accurate for small to medium values of $\mathcal{K}$ (the author uses $\mathcal{K} \leq 3$ in the simulations) and for balanced branches. If the last condition is not met, the asymptotes are accurate only in the high SNR region. In [13], an analysis of systems operating MRC with imperfect channel estimation for Rician fading channels was carried out. Accurate expressions of the BER for M-QAM were derived. The expressions are obtained in terms of some parameters defined based on the decision boundaries of the M-QAM constellation. The authors provide these parameters for 16-QAM and 64-QAM. Unfortunately, the numerical results of the mentioned work do not show unbalanced diversity scenarios. The Rician distribution can be approximated by the Nakagami-m distribution by employing $m = (\mathcal{K}+1)^2/(2\mathcal{K}+1)$ [14]. In [15], expressions to evaluate the SNR and the outage probability of MRC on Nakagami-m fading channels with unequal power branches are determined. Therefore, these results can be used to analyze the MRC performance under unbalanced Rician channels. However, this approach may not be accurate in the high SNR region [16], which is of fundamental importance when analyzing the performance of a system.

First deployments of 5G networks have been made using OFDMA and proposals for new multiple access techniques are also based on OFDMA [17]–[19]. OFDMA based cellular systems are greatly affected by co-cell interference (CCI) [6], [20], which cannot be completely eliminated, but can be reduced using some techniques as smart antenna arrays or channel allocation algorithms [21]–[23]. Therefore, in the literature, the reuse of channels in cells is of extreme importance. The usually adopted approach is hard reuse, where the total bandwidth is split into several sub-bands according to a chosen reuse factor, but it experiences reduced spectral efficiency [24]. As a consequence, some more efficient inter-cell interference coordination (ICIC) techniques have been proposed [25]. One of them is soft frequency reuse (SFR), where the total bandwidth is split into several sub-bands and they are allocated smartly into inner and outer cell regions. In general, as interference in the uplink is greater than that in the downlink [20], the uplink is preferred to analyze the performance of SFR schemes.

Some works have studied cellular systems performance for SFR. In [26], the downlink of a SFR network with hexagonal cells was investigated in terms of the coverage probability, that is defined as the probability of the instantaneous received signal-to-noise-plus-interference ratio (SNIR) is greater than a threshold. In the analysis, a Rayleigh-Lognormal fading channel is assumed. Using approximations for the fading amplitude probability density function (PDF), accurate approximate coverage probability expressions are derived. Expressions of the worst-case signal-to-interference ratio (SIR) of hexagonal SFR cellular systems were obtained in [27], which behave as lower bounds that can be a quite good approximation to the simulations for some specific scenarios, but not in others. In [28], the throughput of hexagonal cellular systems that employs SFR was obtained. Simulations are used for this purpose and the SFR power ratio criterion is considered, i.e., the ratio between the power density in the outer region and in the inner region of each cell. Results show that increasing the power ratio, the average throughput decreases because higher power is employed by users in the outer cell region, which increases CCI. In [29], the system spectral efficiency with SFR is analyzed considering circular cells and omnidirectional antennas at the base stations. Specifically, the impact of the overlapping between adjacent cell areas is studied for long-term-evolution (LTE) systems. Results show that SFR presents better spectral efficiency when the overlapping area is very large or very small. Finally, the coverage probability and the average bit rate were analyzed in [30] considering a SFR cellular system operating in a Nakagami-Lognormal fading channel. Accurate integral-form expressions were derived to evaluate the aforementioned parameters. As evidenced, many recent papers still consider hexagonal or circular cell models, since they are an interesting simple option when the first approach of a particular subject related to cellular systems is carried out.

Another technique to mitigate CCI is sectorization, where the omni-directional antenna at the base station is replaced by directional sector antennas. New sectorization schemes have been proposed so far for OFDMA based systems. In [31], a higher order sectorization scheme where cells are divided into 12 sectors is proposed for fractional-frequency-reuse (FFR). This study shows that the system spectral efficiency is improved by a large number of sectors. A perfect sectorization scenario is considered in this paper. On the other hand, some works consider cellular systems that employ both SFR and sectorization. In [32], expressions to evaluate the SIR of SFR heterogeneous networks were obtained and interference levels from different base station tiers to the users are computed. The analysis was presented for hexagonal and irregular cells assuming ideal sectorization. A multi-layer SFR combined with ideal cell sectorization was proposed in [33] for a three sectorized hexagonal cellular system. Besides,

a spectrum allocation scheme was presented. Results show that spectral efficiency of the outer cell region is improved with the proposal. Finally, in [34], an approach similar to SFR was presented, where the reuse scheme is based on ideal cell sectorization considering that the same channels are used in different sectors of a cell. It is shown that the proposed reuse scheme obtains better performance than non-sectorized SFR.

Other works use SFR and sectorization as model to propose scheduling algorithms to reduce CCI. These works go beyond the scope of this paper, but some references are provided for the reader [35]–[37]. Again, perfect sectorization is assumed in these works, which does not happen in real scenarios due to radiation pattern of commercial antennas. Some proposals that emulate imperfect sectorization can be found in [38]–[42]. In particular, an expression that fits well to real antenna radiation patterns can be found in [41]. In that paper, the BER of multicarrier-code-division-multiple-access (MC-CDMA) systems employing binary-phase-shift-keying (BPSK) modulation and a multiuser maximum likelihood detector is evaluated. The studied scenario has considered Rayleigh fading and non-ideal sectorized hard reuse cellular systems. A hard reuse scheme was also considered in [38]–[40] and in [42] in order to evaluate the performance of different cellular scenarios, that include CDMA and non-orthogonal multiple access (NOMA) systems, respectively.

Finally, an approach to evaluate the spectral efficiency considering that users must present a maximum BER is presented in [43]. This proposal bases the spectral efficiency calculation on the coverage radius of each modulation used in the system can offer so that a target BER is guaranteed. Hence, in order to use this approach, it is first necessary to obtain expressions to evaluate the system BER. In particular, in [43], the cellular spectral efficiency of MC-CDMA systems in hard frequency reuse and Rayleigh fading channel has been evaluated without considering sectorization and diversity.

To the best of our knowledge, a study of cellular systems operating in Rician fading channels with unbalanced diversity branches and in an SFR scenario with imperfect sectorization has not been conducted. Thus, this scenario is assumed in this work to evaluate the BER and the cellular spectral efficiency in the uplink of OFDMA systems that employ M-QAM modulation. Sectorization is modeled based on our approach presented in [41], which emulates imperfect sectorization taking as reference real antenna radiation patterns. In addition, perfect power control is considered in a system where users are uniformly distributed into the cells area. The main contributions of this work are:

- A new analytical approach to model imperfect sectorization in SFR cellular scenarios is proposed, which can be easily extended to other channel reuse mechanisms such as fractional frequency reuse.
- It is determined that CCI sample per branch can be modeled by a zero-mean complex Gaussian random variable. An expression to calculate its variance is obtained, that depends if a user is in the inner or outer cell region.
- An exact expression to calculate the received SNIR per branch is obtained. The moment-generating function (MGF) of this random variable is also determined. Besides, the MGF of the total received SNIR is derived.
- An exact single integral expression to calculate the mean BER of a user is derived. This expression is validated by Monte Carlo simulations.
- A closed-form upper-bound BER expression is obtained. This expression proves accurate approximations to the exact BER in all the SNR regimes.
- Using the derived BER expressions, the proposal of [43] is adapted for our SFR scenario. An algorithm that calculates the coverage radius for each modulation is presented and an expression that evaluates the cellular spectral efficiency is obtained. This proposal allows to look for scenarios that optimize the cellular spectral efficiency and guarantee a maximum BER in both inner and outer cell regions.

This paper is outlined as follows. The list of symbols is shown in Section II. System and channel models are presented in Section III. CCI statistics are analyzed in Section IV. The system performance is analyzed in Section V. Numerical results and discussions are carried out in Section VI and the main conclusions are summarized in Section VII.

II. LIST OF SYMBOLS

Table 1 shows the list of the symbols used in this paper.

III. CHANNEL AND SYSTEM MODELS

The system and channel models are described in this section.

A. SYSTEM MODEL

Before describing the system model, Fig. 1 shows the SFR scheme in a non-sectorized scenario. Typically, 2/3 of the available bandwidth are allocated to the inner region of each cell [30]. However, the bandwidth assigned to each region can vary from cell to cell according to the employed scheduling algorithm [35]–[37]. Moreover, a reuse radius, R_s, (or threshold distance) is used to delimitate inner and outer regions of each cell. This radius is set based on traffic requirements, transmission power, interference levels or other

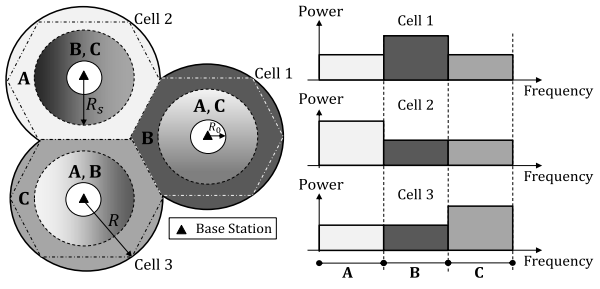

FIGURE 1. Channels allocation in a non-sectorized SFR cellular system.

TABLE 1. List of symbols and notation.

Symbol	Connotation
B_s	subcarrier bandwidth
d_j	distance between j-th co-cell interferer and the BS of interest
D	distance between the center of two co-cells
$\mathrm{E}[\cdot]$	mean operator
f_c	carrier frequency
$\mathcal{G}_1(\varphi)$	antenna gain as a function of φ for the frontal lobe
$\mathcal{G}_2(\varphi)$	antenna gain as a function of φ for the backside lobe
h	complex channel gain
$\mathcal{H}$	ratio between the outer region area and the total cell area
$\mathbf{i}$	imaginary unit, $\mathbf{i} = \sqrt{-1}$
L	number of subcarriers in the OFDMA system
L_p	number of samples used in the cyclic prefix
$p(t)$	Nyquist base-band pulse
$\overline{P_b}$	mean bit error rate
$P_{b,\mathrm{T}}$	target bit error rate
P_r	received power
P_t	transmitted power
$P_{t,\mathrm{M}}$	maximum transmitted power of a user equipment
r	random distance between a user and its serving base station
R	cell radius
R_i	internal radius of a cell region
R_f	external radius of a cell region
R_s	cell reuse radius employed for SFR
$\mathcal{R}_b$	bit rate
$\mathcal{R}_m$	coverage radius for the modulation of order m
$\Re\{\cdot\}$	real operator
T_s	symbol duration
α	fading amplitude
β	path-loss exponent
ϵ	bandwidth and power increase factor due to the cyclic prefix
$\mathcal{K}$	shape parameter of the Rice distribution
μ	mean of a real Gaussian components of the channel gain
ϕ	channel phase
$\Phi_x(s)$	MGF of the random variable x
$\mathcal{P}$	scale parameter of the Rice distribution
φ	angle with which a signal arrives to the base station antenna
θ	angle formed by the horizontal axis and the user position
σ^2	variance of the real random components of the channel gain
σ^2_ζ	CCI variance
σ^2_n	noise variance
$\overline{\xi}$	mean cellular spectral efficiency
$\lvert\cdot\rvert$	modulus operator
$\lfloor\cdot\rfloor$	floor operator
$[x, y]$	value range for a given variable z, i.e., $x \leq z \leq y$

aspects affecting the system performance. The ratio between the outer region area and the total cell area[1] is denoted by $\mathcal{H}$.

Our system model considers SFR, where all cells are circular with an internal radius R_0, an external radius R and a base station (BS) at the cell center. Circular cells with a small hole at their centers ensure convergence in the average received power at the BS. Hence, given $\mathcal{H}$, the reuse radius is

$$R_s = R\left[1 + \left(\frac{R_0^2}{R^2} - 1\right)\mathcal{H}\right]^{\frac{1}{2}}. \tag{1}$$

Fig. 2 shows the cellular scenario, where all CCI comes from the 6 co-cells of the first layer. The influence of outer cell layers over CCI is negligible in urban scenarios [39]. Without loss of generality, cells are divided into 3 sectors in Fig. 2. Each one of the frequency bands A, B and C (refer to Fig. 1) is split into three sub-bands that are allocated

[1]The area of the circle hole with radius R_0 is excluded from the cell area.

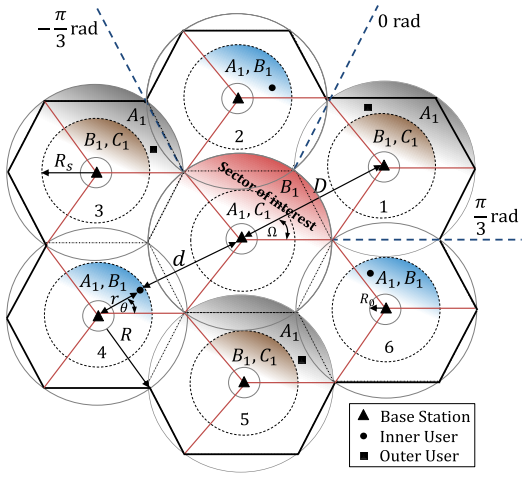

FIGURE 2. Interfering regions in the co-cells for both regions of the sector of interest for the SFR cellular scenario.

to the sectors. For analytical purposes, a sector of interest is assumed and the sub-bands A_1 and B_1 are considered henceforth in the analysis. Hence, notice that the inner region and the outer region of the sector of interest are affected by interference coming from different regions of the co-cells. The inner region is affected by CCI coming from the outer regions of co-cells 1, 3 and 5 (gray regions) and from the inner regions of co-cells 2, 4 and 6 (blue regions). On the other hand, the outer region is affected by CCI coming from the inner regions of all co-cells (brown and blue regions).

It is assumed an OFDMA system where a target user in the sector of interest transmits the same symbol on G different radio channels to obtain diversity.[2] In addition, there is an interferer in each co-cell transmitting on the same radio channels the user of interest transmits. All user equipments (UEs) transmit symbols that belong to a M-QAM constellation with normalized mean power, i.e., $\sigma_s^2 = 1$.

Since users are uniformly distributed in the sector area, the distance between a user and its serving BS, r, is a random variable with PDF

$$f(r; R_\mathrm{i}, R_\mathrm{f}) = \frac{2r}{R_\mathrm{f}^2 - R_\mathrm{i}^2}, \quad R_\mathrm{i} \leq r \leq R_\mathrm{f}, \tag{2}$$

where R_i and R_f are the internal and external radii of a cell region, respectively. Hence, the PDF of r for the inner region is $f(r; R_0, R_s)$ and for the outer region is $f(r; R_s, R)$. Besides, the angle formed by the horizontal axis and the user position is denoted by the random variable θ, whose PDF is

$$f(\theta) = \frac{3}{2\pi}, \quad 0 \leq \theta \leq \frac{2\pi}{3}. \tag{3}$$

Let r_j be the distance between an interferer in the j-th co-cell and its serving BS and θ_j the angle formed by that user location and the horizontal axis. The distance between

[2]The radio channels are subcarriers or time-slots. If the same symbol is transmitted on different subcarriers, frequency diversity is obtained. If the symbol is transmitted on different time-slots, the system gets time diversity.

that interferer and the BS in the cell of interest is

$$d_j \approx \sqrt{D^2 + r_j^2 + 2Dr_j \cos\left[\theta_j - \Omega - (j-1)\frac{\pi}{3}\right]}, \quad (4)$$

where $D = \sqrt{3}R$ is the distance between the center of two co-cells [20] and due to the cellular geometry, the angle $\Omega = \pi/6$ (Refer to Fig. 2). In real scenarios, the exact value of d_j depends also on the BS antenna height (h_a), but as typically $d_j \gg h_a$, (4) is a reasonable analytical approximation.

In [39], imperfect sectorization was emulated assuming an additional opening angle, v, that is added to the set of angles defined for the perfect sector, as shown in Fig. 3. In this figure, the radiation pattern of the commercial antenna Ubiquiti AM9M13 is also shown as an example. In [38] and [40], the radiation pattern is modeled by a parabola, which is a function of the normalized gain at the sector crossover, ϱ_b, and the normalized backside gain, $\mathcal{B}$. This approach is also shown in Fig. 3. In [41], an antenna radiation pattern expression is proposed, where the normalized antenna gain is defined for two angle intervals measured in radians. Let φ be the angle that a signal arrives to the antenna, such that $|\varphi| \leq \pi$ rad. Moreover, let a and b be angles of the radiation pattern, such that $a < b$. For $|\varphi| \leq b$, the antenna gain is given by

$$\mathcal{G}_1(\varphi) = -\Theta(a, b, \varrho_a, \varrho_b, 1)\varphi^2 + \Theta(a, b, \varrho_a, \varrho_b, 2)|\varphi| + 1, \quad (5a)$$

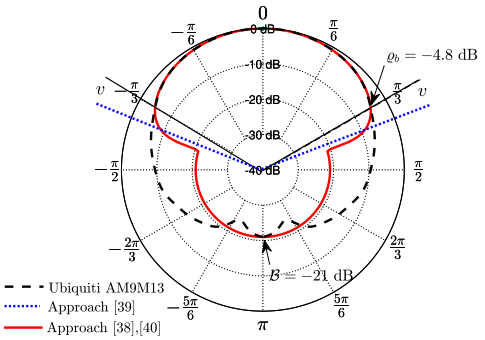

FIGURE 3. Radiation pattern of the commercial antenna Ubiquiti AM9M13 and imperfect sectorization emulation using the approaches of [38]–[40].

but for $|\varphi| > b$ the antenna gain is defined as

$$\mathcal{G}_2(\varphi) = \varrho_b \exp(b^\eta - |\varphi|^\eta), \quad (5b)$$

with

$$\Theta(a, b, \varrho_a, \varrho_b, i) = \frac{a^i(\varrho_b - 1) - b^i(\varrho_a - 1)}{ab(a-b)}, \quad (6)$$

where ϱ_a and ϱ_b are the antenna gains for the angles a and b, respectively, and η is an adjustment factor for the back lobe gain. As in [41], we consider the antenna at the BS has the radiation pattern given by (5a)-(5b), with $b = \pi/3$, which is the ideal sector angle for a cell divided into 3 sectors. Fig. 4 and Fig. 5 show the radiation patterns of the commercial antennas Ubiquiti AM9M13 and Amphenol 6898100, respectively, and the analytical patterns obtained through (5a)-(5b). The analytical radiation pattern shown in Fig. 4 is named pattern $\mathcal{U}$ and it is plotted using $a = \pi/6$ rad, $b = \pi/3$ rad, $\varrho_a = -0.8$ dB, $\varrho_b = -4.8$ dB and $\eta = 1.65$. On the other hand, the radiation pattern shown in Fig. 5 is named pattern $\mathcal{A}$ and it is plotted using $a = \pi/6$ rad, $b = \pi/3$ rad, $\varrho_a = -3.8$ dB, $\varrho_b = -12$ dB and $\eta = 2.7$.

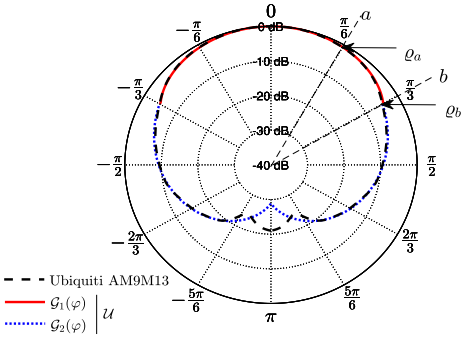

FIGURE 4. Radiation pattern of the commercial antenna Ubiquiti AM9M13 and analytical radiation pattern $\mathcal{U}$.

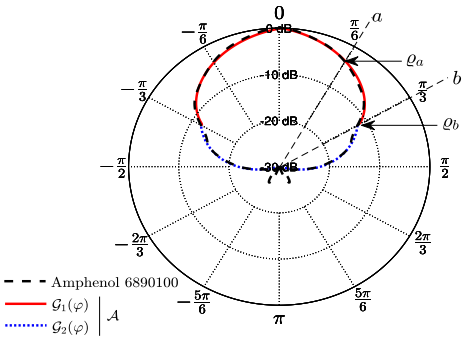

FIGURE 5. Radiation pattern of the commercial antenna Amphenol 6890100 and analytical radiation pattern $\mathcal{A}$.

A system performing perfect power control is assumed [46], [47]. In this scenario, the output power of each UE is

$$P_t = P_{r,0} r^\beta, \quad (7)$$

where $P_{r,0}$ is the constant received power at the BS from all UEs in the same cell and β is the path-loss exponent [20]. Thus, the factor r^β allows the signals transmitted by all UEs to reach the BS with the same power, because, as described in Subsection III-B, the path-loss increases as a power of the distance. The power transmitted by a UE must satisfy $P_t \leq P_{t,\mathrm{M}}$, where $P_{t,\mathrm{M}}$ is the maximum transmit power of a UE. In the receiver at the BS, the signal replicas (diversity branches) are combined using MRC [8]. Finally, perfect channel state information (CSI) is considered.

B. CHANNEL MODEL

The signal replicas are affected by independent channel gains. In particular, the g-th channel gain is modeled as a complex Gaussian random variable, where one of its real components has zero mean, while the other has mean μ_g for $g = 1, 2, \ldots, G$. Moreover, both real components have variance σ^2. Hence, the g-th channel gain can be written as $h = \alpha_g \exp(\mathbf{i}\,\phi_g)$, where ϕ_g is a uniformly distributed phase over $[0, 2\pi), \forall\, g$ and α_g is the fading amplitude, which is modeled by a Rice random variable, whose PDF is [44]

$$f(\alpha_g) = \frac{2(\mathcal{K}_g+1)}{\mathcal{P}_g}\alpha_g \exp\left(-\frac{\mathcal{K}_g+1}{\mathcal{P}_g}\alpha_g^2 - \mathcal{K}_g\right) \times I_0\left(2\sqrt{\frac{\mathcal{K}_g(\mathcal{K}_g+1)}{\mathcal{P}_g}}\alpha_g\right), \quad \alpha \geq 0, \tag{8}$$

where $I_0(\cdot)$ is the modified Bessel function of the first kind and order zero [45, Eq. (9.1.10)],

$$\mathcal{K}_g = \frac{\mu_g^2}{2\sigma^2}, \tag{9}$$

is the shape parameter, i.e., the ratio of the LOS path power to the remaining multipaths power, and the scale parameter

$$\mathcal{P}_g = \mu_g^2 + 2\sigma^2, \tag{10}$$

that is defined as the total power received in all paths, i.e., (10) is the mean squared fading amplitude.

Exponential path-loss is also considered. Hence, the instantaneous received power at the BS from each UE is

$$P_r = \frac{1}{G}P_t r^{-\beta}\sum_{g=1}^{G}|h_g|^2, \tag{11}$$

where P_t is the power transmitted by a UE and r is the distance between that UE and its serving BS. The factor $1/G$ normalizes the power transmitted in each channel (diversity branch). Finally, the signals received by the BS are contaminated by additive white Gaussian noise (AWGN). The noise sample at the correlator (matched filter) output is modeled by a zero-mean complex Gaussian random variable with variance per dimension given by

$$\sigma_n^2 = \frac{N_0}{4T_s}, \tag{12}$$

where N_0 is the unilateral noise power spectral density and T_s is the symbol duration.

IV. CO-CELL INTERFERENCE STATISTICS

In this section, the mean and the variance of the CCI received per channel are obtained.

After demodulation and correlator stages at the BS of interest receiver, the CCI sample for the g-th channel is

$$\mathcal{C}_g = \frac{1}{T_s}\int_0^{T_s} c_g(t)p(t)\exp(-\mathbf{i}\,2\pi f_c t)dt, \tag{13}$$

where $p(t)$ is a base-band pulse satisfying the Nyquist criterion, f_c is the carrier frequency and $c_g(t)$ is the CCI at the antenna input. After considering the antenna radiation pattern, power control and path-loss, $c_g(t)$ can be written as

$$c_g(t) = \frac{1}{\sqrt{G}}\sum_{j=1}^{6}\sqrt{P_t\, r_j^{\beta}\, d_j^{-\beta}\, \mathcal{G}(\varphi_j)} \times \left\{h_{g,j}\Re\left[s_j \exp(\mathbf{i}\,2\pi f_c t)p(t-\tau_j+T_s)\right] + h'_{g,j}\Re\left[s'_j \exp(\mathbf{i}\,2\pi f_c t)p(t-\tau_j)\right]\right\}, \tag{14}$$

where φ_j is the angle between the interferer at the j-th co-cell and the antenna at the BS of interest. A sum of two terms appears inside the braces because CCI is asynchronous. Refer to Fig. 6, where the carrier has been omitted, thus, only base-base signals are shown for simplicity. The first term inside the braces is the CCI sample in the time interval $0 \leq t < \tau_j$ and the second term denotes the sample in the interval $\tau_j \leq t < T_s$, where τ_j is the signal delay of the j-th interferer, that is modeled by a uniform random variable distributed over $[0, T_s]$. Moreover, $h_{g,j}$ and $h'_{g,j}$ are the channel gains affecting the g-th signal replica on the radio link between the j-th interferer and the BS of interest in the intervals $0 \leq t < \tau_j$ and $\tau_j \leq t < T_s$, respectively. Besides, s_j and s'_j are the symbols transmitted by the interferer in the same time intervals, respectively.

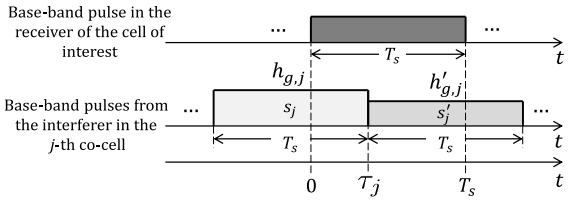

FIGURE 6. Asynchronous signals arriving at the BS of interest.

Substituting (14) in (13), assuming that $p(t)$ is a rectangular base-band pulse with duration T_s and after some manipulations, (13) can be rewritten as

$$\mathcal{C}_g = \frac{1}{2\sqrt{G}}\sum_{j=1}^{6}\sqrt{P_t\, r_j^{\beta}\, d_j^{-\beta}\, \mathcal{G}(\varphi_j)} \times \left\{ R(\tau_j)\,\alpha_{g,j}\left[\left(s_{p,j}\cos\left(\phi_{g,j}\right) - s_{q,j}\sin\left(\phi_{g,j}\right)\right) + \mathbf{i}\left(s_{p,j}\sin\left(\phi_{g,j}\right) + s_{q,j}\cos\left(\phi_{g,j}\right)\right)\right] + R'(\tau_j)\alpha'_{g,j}\left[\left(s'_{p,j}\cos\left(\phi'_{g,j}\right) - s'_{q,j}\sin\left(\phi'_{g,j}\right)\right) + \mathbf{i}\left(s'_{p,j}\sin\left(\phi'_{g,j}\right) + s'_{q,j}\cos\left(\phi'_{g,j}\right)\right)\right]\right\}, \tag{15}$$

where $s_{p,j}$ and $s_{q,j}$ are the in-phase and quadrature components of a symbol, respectively and it was used $h_{g,j} = \alpha_{g,j}\exp(\mathbf{i}\,\phi_{g,j}), h'_{g,j} = \alpha'_{g,j}\exp(\mathbf{i}\,\phi'_{g,j}), R(\tau_j) = \frac{1}{T_s}\int_0^{\tau_j} p(t)p(t-\tau_j-T_s)dt, R'(\tau_j) = \frac{1}{T_s}\int_{\tau_j}^{T_s} p(t)p(t-\tau_j)dt$.

From (15), the CCI is a zero-mean random variable because $\mathrm{E}[s_{p,j}] = \mathrm{E}[s_{q,j}] = \mathrm{E}[s'_{p,j}] = \mathrm{E}[s'_{q,j}] = 0$ and

because[3] $\mathrm{E}[\sin(\phi_{g,j})] = \mathrm{E}[\cos(\phi_{g,j})] = \mathrm{E}[\sin(\phi'_{g,j})] = \mathrm{E}[\cos(\phi'_{g,j})] = 0$. Hence, after some manipulations of (15), it can be shown that the CCI variance per channel is given by

$$\sigma_c^2 = \frac{1}{12G} P_t\, \sigma_s^2\, \mathcal{P}_c \sum_{j=1}^{6} \mathrm{E}\left[r_j^{\beta} d_j^{-\beta} \mathcal{G}(\varphi_j)\right], \tag{16}$$

where we used[3] $\mathrm{E}[\sin^2(x)] = 1/2$ and $\mathrm{E}[\sin(x)\cos(y)] = 0$, for x and y independent and identically distributed uniform random variables over $[0, 2\pi)$, $\sigma_s^2 = \mathrm{E}[s_{p,j}^2] + \mathrm{E}[s_{q,j}^2] = \mathrm{E}[s_{p,j}'^2] + \mathrm{E}[s_{q,j}'^2]$ and $\mathrm{E}[R^2(\tau_j)] = \mathrm{E}[R'^2(\tau_j)] = 1/3$ because τ_j and τ_j' are uniformly distributed random variables over the interval $[0, T_s]$. Finally, $\mathcal{P}_c$ denotes the fading mean power. Thus, we have assumed that the fading mean power of all co-cell interferers is the same for all g and j, which is acceptable considering that all interferers are far from the BS of interest and hence, the fading mean power, defined in (10), does not change significantly for each interferer.

The CCI variance depends on the regions of the sectors in the co-cells in which interference is generated. Hence, from (2)-(6), the factor $\mathrm{E}\left[r_j^{\beta} d_j^{-\beta} \mathcal{G}(\varphi_j)\right]$, in (16), can be written as a function that depends on some parameters, that is,

$$\begin{aligned}\mathrm{E}\left[r_j^{\beta} d_j^{-\beta} \mathcal{G}(\varphi_j)\right] &= \Psi(j,k;\theta_1,\theta_2;\varphi_j;r_1,r_2;R_{\mathrm{i}},R_{\mathrm{f}};\beta)\\ &= \int_{\theta_1}^{\theta_2}\int_{r_1}^{r_2} \mathcal{G}_k(\varphi_j)\,\mathcal{J}(r,\theta,j,\beta)\\ &\quad \times f(r;R_{\mathrm{i}},R_{\mathrm{f}}) f(\theta) dr d\theta,\end{aligned} \tag{17}$$

where j is the co-cell number, $k \in \{1, 2\}$ is the antenna gain, that is, $\mathcal{G}_1$ given by (5a) or $\mathcal{G}_2$ given by (5b), $[\theta_1, \theta_2]$ is the angle interval where interferers are into their cells, φ_j is the random angle between the j-th co-cell interferer and the BS antenna of interest, $[r_1, r_2]$ is the distance interval between interferers and their serving BSs, R_{i} and R_{f} are the internal and external radii of the interferer region in the j-th co-cell, respectively, and with (4), the following function is defined

$$\mathcal{J}(r,\theta,j,\beta) = \left\{\frac{r^2}{D^2 + r^2 + 2Dr\cos\left[\theta - \Omega - (j-1)\frac{\pi}{3}\right]}\right\}^{\frac{\beta}{2}}, \tag{18}$$

which represents the product $r_j^{\beta} d_j^{-\beta}$. As can be noticed, the above expression is a function of r, θ, j and β. Moreover, from Subsection III-A, we have that $\Omega = \pi/6$ rad.

The CCI variance for each region in the sector of interest is calculated in the following. In particular, the parameters defined by (17) are obtained. With these results, the CCI variance can be easily calculated using (16).

A. CCI VARIANCE FOR THE INNER REGION OF THE SECTOR OF INTEREST

According to Subsection III-A, the frequency sub-band A_1 is used in the analysis of the inner region.

[3]The phases $\phi_{g,j}$ and $\phi'_{g,j}$ are independent and identically distributed uniform random variables over the interval $[0, 2\pi)$, $\forall g, j$.

Superimposing Fig. 2 and Fig. 4 (or Fig. 5), we observe that signals arriving at the BS of interest from co-cells 1 and 2 reach the antenna radiation pattern at the $\mathcal{G}_1(\varphi)$ gain region. Signals from co-cells 4 and 5 arrive at the $\mathcal{G}_2(\varphi)$ gain region and signals from co-cells 3 and 6 reach regions where the antenna gain is of the type $\mathcal{G}_1(\varphi)$ or $\mathcal{G}_2(\varphi)$.

Without loss of generality, co-cells $j = 1, 3$ and 6 are used as examples in the following analysis. First, let us determine φ_j. For this, consider Fig. 7 and Fig. 8, where B_0 is the BS of interest and B_j is the BS of co-cell j. Using (4), we can find that the angle $\omega(r, \theta, j)$ in these figures is given by

$$\omega(r,\theta,j) = \cos^{-1}\left\{\frac{D + r\cos\left[\theta - \Omega - (j-1)\frac{\pi}{3}\right]}{\sqrt{D^2 + r^2 + 2Dr\cos\left[\theta - \Omega - (j-1)\frac{\pi}{3}\right]}}\right\}. \tag{19}$$

In Fig. 7 and Fig. 8, ψ_j is the angle formed by the line connecting B_0 and the BS of the j-th co-cell and the horizontal axis. This angle is $\psi_j = \Omega + (j-1)\pi/3, \forall j$. In addition, ϑ_j is the angle formed by the line connecting B_0 and the interferer in the j-th co-cell and the horizontal axis. For the specific case of co-cell $j = 1$, the angle ϑ_j is obtained as

$$\vartheta_1 = \begin{cases} \psi_1 - \omega(r,\theta,1), & 0 \le \theta \le \Omega \\ \psi_1 + \omega(r,\theta,1), & \Omega < \theta \le \dfrac{2\pi}{3}. \end{cases} \tag{20}$$

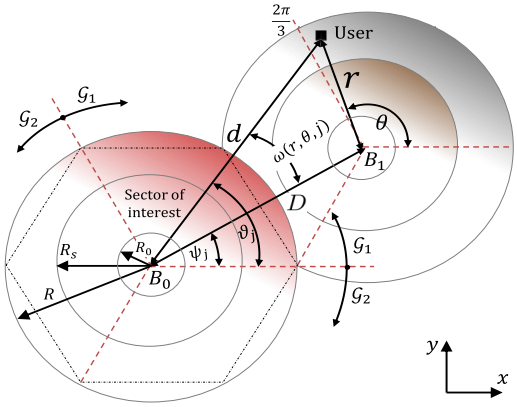

FIGURE 7. Geometric parameters for co-cell 1.

As a consequence, considering the 0 radians reference of Fig. 2, the random angle φ_j, for $j = 1$, is given by

$$\varphi_1 = \begin{cases} -\Omega + \omega(r,\theta,1) + \dfrac{\pi}{3}, & 0 \le \theta \le \Omega \\ -\Omega - \omega(r,\theta,1) + \dfrac{\pi}{3}, & \Omega < \theta \le \dfrac{2\pi}{3}. \end{cases} \tag{21}$$

In (21), the interval limits for θ define the values for θ_1 and θ_2, which are used in (17). Similar procedure can be performed for the other co-cells. Table 2 indicates the angle φ_j for the j-th co-cell and the θ interval.

The next step is to find the integration intervals of θ and r in (17), i.e., $[\theta_1, \theta_2]$ and $[r_1, r_2]$, respectively, for each co-cell.

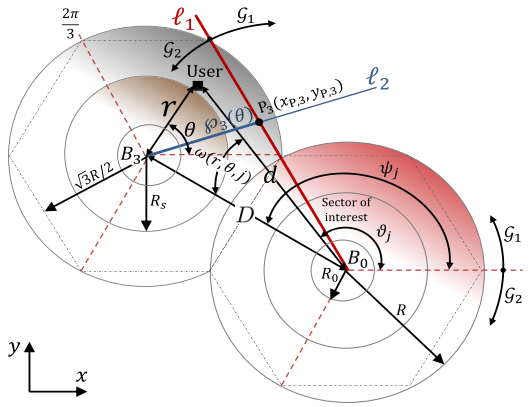

FIGURE 8. Geometric parameters for co-cell 3 considering that $R_s \leq \sqrt{3}R/2$.

TABLE 2. Angle φ_j as a function of j and the θ interval.

j	θ interval, $[\theta_1, \theta_2]$	φ_j
1	$[0, \Omega]$	$-\Omega + \omega(r,\theta,1) + \pi/3$
	$[\Omega, 2\pi/3]$	$-\Omega - \omega(r,\theta,1) + \pi/3$
2	$[0, \Omega + \pi/3]$	$-\Omega + \omega(r,\theta,2)$
	$[\Omega + \pi/3, 2\pi/3]$	$-\Omega - \omega(r,\theta,2)$
3	$[0, 2\pi/3]$	$-\Omega + \omega(r,\theta,3) - \pi/3$
4	$[0, \Omega]$	$-\Omega - \omega(r,\theta,4) - 2\pi/3$
	$[\Omega, 2\pi/3]$	$-\Omega + \omega(r,\theta,4) - 2\pi/3$
5	$[0, \Omega + \pi/3]$	$-\Omega - \omega(r,\theta,5) + \pi$
	$[\Omega + \pi/3, 2\pi/3]$	$-\Omega + \omega(r,\theta,5) + \pi$
6	$[0, 2\pi/3]$	$-\Omega - \omega(r,\theta,6) + 2\pi/3$

CCI from co-cell $j = 1$, that affects the sector of interest inner region, is generated by the outer region of this co-cell. From Fig. 7, the integration interval for r is $[R_s, R]$ because the interferer is in the outer region of this co-cell. In the figure, notice also that the antenna gain is always $\mathcal{G}_1$ for the CCI arriving from this co-cell, thus, $k = 1$ is used in (17).

The outer region of co-cell $j = 3$ also produces CCI for the inner region of the sector of interest. In this case, the integral defined in (17) is calculated in some intervals, which depend on the value of R_s. This is explained in the following. Fig. 8 shows the scenario for $R_s \leq \sqrt{3}R/2$. Specifically, $\sqrt{3}R/2$ is the radius of the circle inscribed in the hexagon, that is, its apothem. In this figure,[4] $\wp_3(\theta)$ is the line segment connecting BS B_3 and the line ℓ_1. The segment length is a function of θ. Observe in the figure that for $0 \leq \theta \leq \pi/3$, the first integration interval for r is $\wp_3(\theta) \leq r \leq R$ and the antenna gain is $\mathcal{G}_1$, hence, $k = 1$. The second integration interval for r is $R_s \leq r \leq \wp_3(\theta)$. In this case, the same θ interval is considered and the antenna gain is $\mathcal{G}_2$, that is, $k = 2$. Finally, for $\pi/3 \leq \theta \leq 2\pi/3$, the integration interval for r is $R_s \leq r \leq R$.

From the previous analysis, our aim now is to find the length of the line segment $\wp_3(\theta)$. Assume that B_0 is a point in the plane with coordinates $(0, 0)$. Then, due to the hexagonal geometry, B_3 is a point with coordinates $(-\sqrt{3}D/2, D/2)$.

[4]The subscript 3 in $\wp$ and in the other variables refers to co-cell 3.

In addition, the line ℓ_1 passes through the point $(0, 0)$ and has a slope $\tan(2\pi/3) = -\sqrt{3}$. Consequently, the equation of this line is $\ell_1 : y = -\sqrt{3}x$. On the other hand, the line passing through the segment $\wp_3(\theta)$ has a slope that depends on θ, specifically, its slope is $\tan(\theta)$. Hence, the equation of this line is $\ell_2 : y = x\tan(\theta) + D[1 + \sqrt{3}\tan(\theta)]/2$. Solving the system formed by ℓ_1 and ℓ_2, we can get the coordinates of point P_3, that is, $x_{P,3}$ and $y_{P,3}$ (Refer to Fig. 8).

Finally, the length of $\wp_3(\theta)$ is given by the distance between P_3 and B_3, that is,

$$\wp_3(\theta) = \left[\left(x_{P,3} + \frac{\sqrt{3}}{2}D\right)^2 + \left(y_{P,3} - \frac{D}{2}\right)^2\right]^{1/2}, \quad (22)$$

with $x_{P,3} = -D\zeta_3(\theta)/2$, and $y_{P,3} = \sqrt{3}D\zeta_3(\theta)/2$, where

$$\zeta_3(\theta) = \left[\sqrt{3}\tan(\theta) + 1\right]\left[\sqrt{3} + \tan(\theta)\right]^{-1}. \quad (23)$$

Fig. 9 shows co-cell 3 in the scenario where $R_s > \sqrt{3}R/2$. In order to define the integration intervals for the CCI calculation, the angles $\chi_{3,1}$ and $\chi_{3,2}$, which are shown in this figure, must be determined. These angles can be found from the slopes of lines ℓ_3 and ℓ_4, respectively. In order to determine these slopes, the intersection points of the circumference C_3 and the line ℓ_1 should be found. Carrying out this procedure, it is possible to obtain that

$$\chi_{3,a} = \tan^{-1}\left\{\frac{\sqrt{3}\left[1 + (-1)^a\sqrt{4(R_s/R)^2 - 3}\right]}{3 - (-1)^a\sqrt{4(R_s/R)^2 - 3}}\right\}, \quad (24)$$

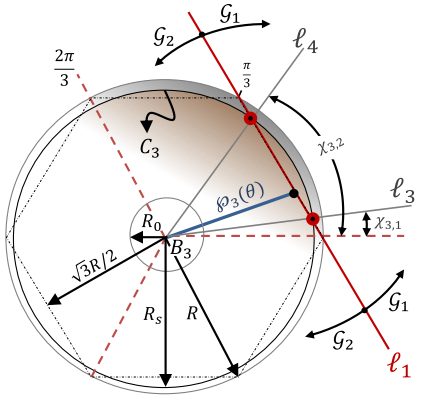

FIGURE 9. Geometric parameters for co-cell 3 considering $R_s > \sqrt{3}R/2$.

for $a \in \{1, 2\}$. From the above analysis and from Fig. 9, notice that the integration intervals of (17) in this scenario are those indicated in Table 3.

The analysis of co-cell 6 is similar to that of co-cell 3. In particular, the interference reaching the sector of interest inner region comes from the inner region of co-cell 6. For $R_s \leq \sqrt{3}R/2$, the double-integral of (17) is computed in the intervals $[0, 2\pi/3]$ and $[R_0, R_s]$ for θ and r, respectively. On the other hand, for $R_s > \sqrt{3}R/2$, the analysis is more

TABLE 3. Integration intervals for (17) considering the CCI generated in the outer region of co-cell 3 when $R_s > \sqrt{3}R/2$.

θ interval, $[\theta_1, \theta_2]$	r interval, $[r_1, r_2]$	Antenna Gain
$[0, \chi_{3,1}]$	$[R_s, \wp_3(\theta)]$	$\mathcal{G}_2,\ k=2$
	$[\wp_3(\theta), R]$	$\mathcal{G}_1,\ k=1$
$[\chi_{3,1}, \chi_{3,2}]$	$[R_s, R]$	$\mathcal{G}_1,\ k=1$
$[\chi_{3,2}, \pi/3]$	$[\wp_3(\theta), R]$	$\mathcal{G}_1,\ k=1$
	$[R_s, \wp_3(\theta)]$	$\mathcal{G}_2,\ k=2$
$[\pi/3, 2\pi/3]$	$[R_s, R]$	$\mathcal{G}_2,\ k=2$

complex. For this, consider Fig. 10, where $\wp_6(\theta)$ is a line segment with length

$$\wp_6(\theta) = \left[\left(x_{\mathrm{P},6} - \frac{\sqrt{3}}{2}D\right)^2 + \left(y_{\mathrm{P},6} + \frac{D}{2}\right)^2\right]^{1/2}, \quad (25)$$

where $x_{\mathrm{P},6} = -D\left\{\sqrt{3} + [\tan(\theta)]^{-1}\right\}/2$ and $y_{\mathrm{P},6} = 0$. Moreover, the angles $\chi_{6,1}$ and $\chi_{6,2}$ are obtained from

$$\chi_{6,a} = (a-1)\pi + \tan^{-1}\left[(-1)^{a-1}\left(\frac{4}{3}\frac{R_s^2}{R^2} - 1\right)^{-\frac{1}{2}}\right], \quad (26)$$

for $a \in \{1, 2\}$. From Fig. 10, the integration intervals of (17) for co-cell 6 are those indicated in Table 4.

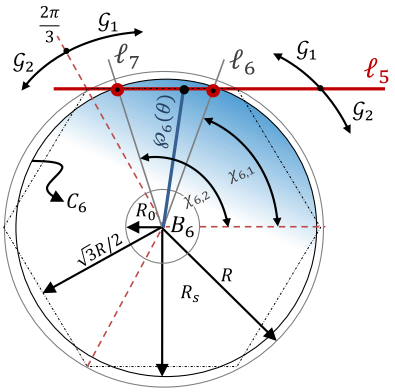

FIGURE 10. Geometric parameters for co-cell 6 considering $R_s > \sqrt{3}R/2$.

TABLE 4. Integration intervals for (17) considering the CCI generated in the inner region of co-cell 6 when $R_s > \sqrt{3}R/2$.

θ interval, $[\theta_1, \theta_2]$	r interval, $[r_1, r_2]$	Antenna Gain
$[0, \chi_{6,1}]$	$[R_0, R_s]$	$\mathcal{G}_2,\ k=2$
$[\chi_{6,1}, \chi_{6,2}]$	$[R_0, \wp_6(\theta)]$	$\mathcal{G}_2,\ k=2$
	$[\wp_6(\theta), R_s]$	$\mathcal{G}_1,\ k=1$
$[\chi_{6,2}, 2\pi/3]$	$[R_0, R_s]$	$\mathcal{G}_2,\ k=2$

The analysis for co-cells 2, 4 and 5 does not depend on R_s. From the results of Tab. 2 and doing an analysis similar to that performed previously, the term $\mathrm{E}[r_j^{\beta} d_j^{-\beta} \mathcal{G}(\varphi_j)]$ used in (16) can be calculated for all 6 co-cells, i.e., for $j = 1, 2, \ldots, 6$. Table 5 shows how these terms are calculated using the function $\Psi(\cdot)$, defined in (17), based on the R_s range.

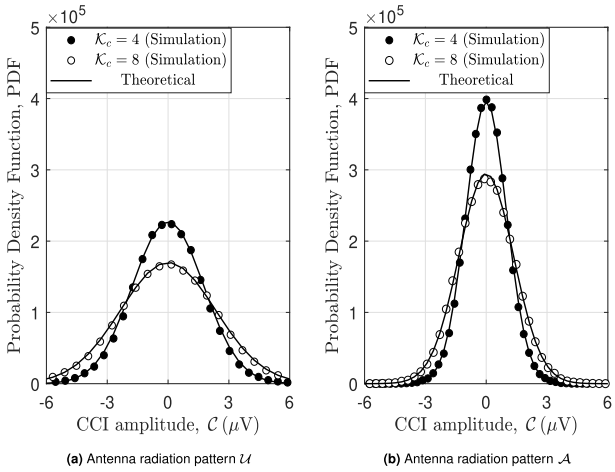

FIGURE 11. PDF of the CCI amplitude that affects the inner region of the sector of interest parameterized by the antenna radiation pattern and $\mathcal{K}_c$, employing $\beta = 4$, $R_0 = 20$ m, $R_s = 800$ m and $R = 1000$ m and $P_t = 23$ dBm.

B. CCI VARIANCE FOR THE OUTER REGION OF THE SECTOR OF INTEREST

From Subsection III-A, the frequency sub-band B_1 is used in the analysis of the outer region of the sector of interest.

The CCI reaching the sector of interest outer region comes from all co-cells inner regions. Thus, superimposing Fig. 2 and Fig. 4 (or Fig. 5) and considering that $R_s \leq \sqrt{3}R/2$, notice that the interference from co-cells 1 and 2 reach the BS antenna pattern at the $\mathcal{G}_1(\varphi)$ gain zone. On the other hand, the interference from co-cells 3, 4, 5 and 6 arrive at the $\mathcal{G}_2(\varphi)$ gain zone. Additionally, due to the geometry, the angles φ_j for the outer region are the same indicated in Table 2. Consequently, the integration intervals of θ, in (17), are known for each co-cell. Besides, as the CCI of the sector of interest outer region comes from all co-cells inner regions, the integration interval of r for all co-cells is $[R_0, R_s]$.

On the other hand, for $R_s > \sqrt{3}R/2$, the analysis changes only for co-cells 3 and 6. From Fig. 9, the integration intervals of (17), for co-cell 3, are those indicated in Table 6. For co-cell 6, the analysis is the same of the previous subsection, where the integration intervals are those shown in Table 4.

By the above, the terms $\mathrm{E}\left[r_j^{\beta} d_j^{-\beta} \mathcal{G}(\varphi_j)\right]$, used in (16), can be easily calculated. Table 7 shows how these terms are obtained using (17) based on the R_s range.

To validate our analysis, Fig. 11 shows the PDF of the CCI affecting the sector of interest inner region parameterized by the antenna and by $\mathcal{K}_c$. The analytical radiation patterns of Fig. 4 and Fig. 5 are used in Fig. 11a and Fig. 11b, respectively. Besides, we used $\beta = 4$, $R_0 = 20$ m, $R_s = 800$m, $R = 1000$ m and $P_t = 23$ dBm[5] and only the CCI in-phase component is considered. Theoretical PDFs have been plotted using the PDF of a zero-mean Gaussian random

[5]The maximum transmission power of Long Term Evolution (LTE) class-3 terminals is 23 dBm [48].

TABLE 5. Calculation of the term $\mathrm{E}\left[r_j^{\beta} d_j^{-\beta} \mathcal{G}(\varphi_j)\right]$ for the j-th co-cell considering the inner region of the sector of interest.

j	$\mathrm{E}\left[r_j^{\beta} d_j^{-\beta} \mathcal{G}(\varphi_j)\right] = \Psi(j,k;\theta_1,\theta_2;\varphi_j;r_1,r_2;R_{\mathrm{i}},R_{\mathrm{f}};\beta)$	R_s Range
1	$\Psi[1,1;0,\Omega;-\Omega+\omega(r,\theta,1)+\pi/3;R_s,R;R_s,R;\beta]+\Psi[1,1;\Omega,2\pi/3;-\Omega-\omega(r,\theta,1)+\pi/3;R_s,R;R_s,R;\beta]$	$[R_0,R]$
2	$\Psi[2,1;0,\Omega+\pi/3;-\Omega+\omega(r,\theta,2);R_0,R_s;R_0,R_s;\beta]+\Psi[2,1;\Omega+\pi/3,2\pi/3;-\Omega-\omega(r,\theta,2);R_0,R_s;R_0,R_s;\beta]$	$[R_0,R]$
3	$\Psi[3,1;0,\pi/3;-\Omega+\omega(r,\theta,3)-\pi/3;\wp_3(\theta),R;R_s,R;\beta]+\Psi[3,2;0,\pi/3;-\Omega+\omega(r,\theta,3)-\pi/3;R_s,\wp_3(\theta);R_s,R;\beta]$ $+\Psi[3,2;\pi/3,2\pi/3;-\Omega+\omega(r,\theta,3)-\pi/3;R_s,R;R_s,R;\beta]$	$\left[R_0,\frac{\sqrt{3}}{2}R\right]$
	$\Psi[3,2;0,\chi_{3,1};-\Omega+\omega(r,\theta,3)-\pi/3;R_s,\wp_3(\theta);R_s,R;\beta]+\Psi[3,1;0,\chi_{3,1};-\Omega+\omega(r,\theta,3)-\pi/3;\wp_3(\theta),R;R_s,R;\beta]$ $+\Psi[3,1;\chi_{3,1},\chi_{3,2};-\Omega+\omega(r,\theta,3)-\pi/3;R_s,R;R_s,R;\beta]+\Psi[3,2;\chi_{3,2},\pi/3;-\Omega+\omega(r,\theta,3)-\pi/3;R_s,\wp_3(\theta);R_s,R;\beta]$ $+\Psi[3,1;\chi_{3,2},\pi/3;-\Omega+\omega(r,\theta,3)-\pi/3;\wp_3(\theta),R;R_s,R;\beta]+\Psi[3,2;\pi/3,2\pi/3;-\Omega+\omega(r,\theta,3)-\pi/3;R_s,R;R_s,R;\beta]$	$\left[\frac{\sqrt{3}}{2}R,R\right]$
4	$\Psi[4,2;0,\Omega;-\Omega-\omega(r,\theta,4)-2\pi/3;R_0,R_s;R_0,R_s;\beta]+\Psi[4,2;\Omega,2\pi/3;-\Omega+\omega(r,\theta,4)-2\pi/3;R_0,R_s;R_0,R_s;\beta]$	$[R_0,R]$
5	$\Psi[5,2;0,\Omega+\pi/3;-\Omega-\omega(r,\theta,5)+\pi;R_s,R;R_s,R;\beta]+\Psi[5,2;\Omega+\pi/3,2\pi/3;-\Omega+\omega(r,\theta,5)+\pi;R_s,R;R_s,R;\beta]$	$[R_0,R]$
6	$\Psi[6,2;0,2\pi/3;-\Omega-\omega(r,\theta,6)+2\pi/3;R_0,R_s;R_0,R_s;\beta]$	$\left[R_0,\frac{\sqrt{3}}{2}R\right]$
	$\Psi[6,2;0,\chi_{6,1};-\Omega-\omega(r,\theta,6)+2\pi/3;R_0,R_s;R_0,R_s;\beta]$ $+\Psi[6,2;\chi_{6,1},\chi_{6,2};-\Omega-\omega(r,\theta,6)+2\pi/3;R_0,\wp_6(\theta);R_0,R_s;\beta]$ $+\Psi[6,1;\chi_{6,1},\chi_{6,2};-\Omega-\omega(r,\theta,6)+2\pi/3;\wp_6(\theta),R_s;R_0,R_s;\beta]+\Psi[6,2;\chi_{6,2},2\pi/3;-\Omega-\omega(r,\theta,6)+2\pi/3;R_0,R_s;R_0,R_s;\beta]$	$\left[\frac{\sqrt{3}}{2}R,R\right]$

TABLE 6. Integration intervals for (17) considering the CCI generated in the inner region of co-cell 3 when $R_s > \sqrt{3}R/2$.

θ interval, $[\theta_1,\theta_2]$	r interval, $[r_1,r_2]$	Antenna Gain
$[0,\chi_{3,1}]$	$[R_0,R_s]$	$\mathcal{G}_2,\ k=2$
$[\chi_{3,1},\chi_{3,2}]$	$[R_0,\wp_3(\theta)]$	$\mathcal{G}_2,\ k=2$
	$[\wp_3(\theta),R_s]$	$\mathcal{G}_1,\ k=1$
$[\chi_{3,2},2\pi/3]$	$[R_0,R_s]$	$\mathcal{G}_2,\ k=2$

variable with variance[6] $\sigma_c^2/2$, where σ_c^2 is obtained from (16). By the central limit theorem [44], the CCI received amplitude can be approximated by a Gaussian random variable. This approximation is adequate for any $\mathcal{K}_c$ and for any antenna.

Although two commercial antennas have been considered in the analysis, the antenna selection depends exclusively on coverage planning. Thus, one antenna is not better than another, that is, network planners choose the antenna based on coverage requirements and on allowed interference levels.

V. PERFORMANCE ANALYSIS

The system performance is evaluated in this section in terms of the mean BER and the mean cellular spectral efficiency.

[6]The variance is divided by 2 because only the in-phase component of the CCI amplitude is considered.

A. MEAN BIT ERROR RATE

An exact mean BER expression is derived in this subsection. Then, a closed-form upper-bound is also obtained.

Let S denotes the signal received at the BS of interest from the k-th user, i.e., the target user, into the sector of interest. Hence, the instantaneous SNIR of the g-th combiner branch can be written as

$$\gamma_g = \frac{S^2}{2(\sigma_n^2+\sigma_c^2)} = \frac{P_t s_k}{8(\sigma_n^2+\sigma_c^2)}\alpha_{g,k}^2, \tag{27}$$

with $S = \sqrt{P_t}s_k\alpha_{g,k}/2$, where s_k is the symbol transmitted by the target user, $\alpha_{g,k}$ is the instantaneous fading amplitude affecting the g-th signal replica and the factor $1/2$ appears due to the modulation/demodulation process. Moreover, σ_n^2 and σ_c^2 are the noise and CCI variances, respectively. Once $\alpha_{g,k}$ is a Rice random variable with PDF given by (8), the MGF of the random variable γ_g is given by

$$\Phi_{\gamma_g}(s) = \exp\left(\frac{\mu_g^2\Delta s}{1-2\sigma^2\Delta s}\right)\left(1-2\sigma^2\Delta s\right)^{-1}, \tag{28}$$

with

$$\Delta = \left\{\frac{2}{3}\mathcal{P}_c\sum_{j=1}^{6}\mathrm{E}\left[r_j^{\beta}d_j^{-\beta}\mathcal{G}(\varphi_j)\right]+\frac{N_0}{E_b}\frac{1}{\log_2 M}\right\}^{-1}, \tag{29}$$

TABLE 7. Calculation of the term $\mathrm{E}\left[r_j^{\beta} d_j^{-\beta} \mathcal{G}(\varphi_j)\right]$ for the j-th co-cell considering the outer region of the sector of interest.

j	$\mathrm{E}\left[r_j^{\beta} d_j^{-\beta} \mathcal{G}(\varphi_j)\right] = \Psi(j,k;\theta_1,\theta_2;\varphi_j;r_1,r_2;R_{\mathrm{i}},R_{\mathrm{f}};\beta)$	R_s range
1	$\Psi[1,1;0,\Omega;-\Omega+\omega(r,\theta,1)+\pi/3;R_0,R_s;R_0,R_s;\beta]+\Psi[1,1;\Omega,2\pi/3;-\Omega-\omega(r,\theta,1)+\pi/3;R_0,R_s;R_0,R_s;\beta]$	$[R_0,R]$
2	$\Psi[2,1;0,\Omega+\pi/3;-\Omega+\omega(r,\theta,2);R_0,R_s;R_0,R_s;\beta]+\Psi[2,1;\Omega+\pi/3,2\pi/3;-\Omega-\omega(r,\theta,2);R_0,R_s;R_0,R_s;\beta]$	$[R_0,R]$
3	$\Psi[3,2;0,2\pi/3;-\Omega+\omega(r,\theta,3)-\pi/3;R_0,R_s;R_0,R_s;\beta]$	$\left[R_0,\frac{\sqrt{3}}{2}R\right]$
	$\Psi[3,2;0,\chi_{3,1};-\Omega+\omega(r,\theta,3)-\pi/3;R_0,R_s;R_0,R_s;\beta]+\Psi[3,2;\chi_{3,1},\chi_{3,2};-\Omega+\omega(r,\theta,3)-\pi/3;R_0,\wp3;R_0,R_s;\beta]$ $+\Psi[3,1;\chi_{3,1},\chi_{3,2};-\Omega+\omega(r,\theta,3)-\pi/3;\wp3,R_s;R_0,R_s;\beta]+\Psi[3,2;\chi_{3,2},2\pi/3;-\Omega+\omega(r,\theta,3)-\pi/3;R_0,R_s;R_0,R_s;\beta]$	$\left[\frac{\sqrt{3}}{2}R,R\right]$
4	$\Psi[4,2;0,\Omega;-\Omega-\omega(r,\theta,4)-2\pi/3;R_0,R_s;R_0,R_s;\beta]+\Psi[4,2;\Omega,2\pi/3;-\Omega+\omega(r,\theta,4)-2\pi/3;R_0,R_s;R_0,R_s;\beta]$	$[R_0,R]$
5	$\Psi[5,2;0,\Omega+\pi/3;-\Omega-\omega(r,\theta,5)+\pi;R_0,R_s;R_0,R_s;\beta]+\Psi[5,2;\Omega+\pi/3,2\pi/3;-\Omega+\omega(r,\theta,5)+\pi;R_0,R_s;R_0,R_s;\beta]$	$[R_0,R]$
6	$\Psi[6,2;0,2\pi/3;-\Omega-\omega(r,\theta,6)+2\pi/3;R_0,R_s;R_0,R_s;\beta]$	$\left[R_0,\frac{\sqrt{3}}{2}R\right]$
	$\Psi[6,2;0,\chi_{6,1};-\Omega-\omega(r,\theta,6)+2\pi/3;R_0,R_s;R_0,R_s;\beta]$ $+\Psi[6,2;\chi_{6,1},\chi_{6,2};-\Omega-\omega(r,\theta,6)+2\pi/3;R_0,\wp_6(\theta);R_0,R_s;\beta]$ $+\Psi[6,1;\chi_{6,1},\chi_{6,2};-\Omega-\omega(r,\theta,6)+2\pi/3;\wp_6(\theta),R_s;R_0,R_s;\beta]+\Psi[6,2;\chi_{6,2},2\pi/3;-\Omega-\omega(r,\theta,6)+2\pi/3;R_0,R_s;R_0,R_s;\beta]$	$\left[\frac{\sqrt{3}}{2}R,R\right]$

where (9), (10), (12) and (16) were employed. In addition, we have used that $\mathrm{E}[s_k^2] = \sigma_s^2 = 1$, that the received energy per symbol is $E_s = P_t T_s/2$ and that the received energy per bit is $E_b = E_s/\log_2 M$, where M is the modulation order.

For MRC, the total received SNIR is obtained as $\Gamma = \sum_{g=1}^{G} \gamma_g$ [8]. Therefore, it is straightforward to show that the MGF of the random variable Γ is

$$\Phi_\Gamma(s) = \prod_{g=1}^{G} \Phi_{\gamma_g}(s), \tag{30}$$

where $\Phi_{\gamma_g}(s)$ is given by (28).

From the results of [49, Eqs. (14), (16)] and [50, Section 5.1], it is possible to determine that the exact mean BER of a system employing MRC and M-QAM is given by

$$\overline{P_b} = \frac{2}{\sqrt{M}\log_2\sqrt{M}} \sum_{\ell=1}^{\log_2\sqrt{M}} \sum_{\kappa=0}^{(1-2^{-\ell})\sqrt{M}-1} (-1)^{\left\lfloor \frac{\kappa 2^{\ell-1}}{\sqrt{M}} \right\rfloor} \times \left(2^{\ell-1} - \left\lfloor \frac{\kappa 2^{\ell-1}}{\sqrt{M}} + \frac{1}{2} \right\rfloor\right) \underbrace{\frac{1}{\pi}\int_0^{\pi/2} \Phi_\Gamma\left(-\frac{\nu_\kappa}{\sin^2 x}\right) dx}_{\mathcal{I}}, \tag{31}$$

where

$$\nu_\kappa = \frac{3(2\kappa+1)^2}{2(M-1)}. \tag{32}$$

Unfortunately, $\mathcal{I}$ has no closed-form for our scenario. Nevertheless, an upper bound for this integral is obtained in Appendix. Hence, from (46) and (47), the upper-bound of the mean BER for our system model is given by

$$\overline{P_b} \leq \frac{2}{\sqrt{M}\log_2\sqrt{M}} \sum_{\ell=1}^{\log_2\sqrt{M}} \sum_{\kappa=0}^{(1-2^{-\ell})\sqrt{M}-1} (-1)^{\left\lfloor \frac{\kappa 2^{\ell-1}}{\sqrt{M}} \right\rfloor} \times \left(2^{\ell-1} - \left\lfloor \frac{\kappa 2^{\ell-1}}{\sqrt{M}} + \frac{1}{2} \right\rfloor\right) \exp\left(-\frac{m_\kappa}{1+m_\kappa} \sum_{g=1}^{G} \mathcal{K}_g\right) \times \left(\frac{1-\rho_\kappa}{2}\right)^G \sum_{j=0}^{G-1} \binom{G-1+j}{j} \left(\frac{1+\rho_\kappa}{2}\right)^j, \tag{33}$$

where

$$m_\kappa = 2\sigma^2 \Delta \nu_\kappa, \tag{34}$$

and

$$\rho_\kappa = \sqrt{\frac{m_\kappa}{1+m_\kappa}}. \tag{35}$$

In (29), notice that as the E_b/N_0 ratio tends to infinity, then Δ does not depend on this parameter anymore, once N_0/E_b tends to zero. Therefore, as (31) and (33) depend on Δ, we conclude that, at high SNR, the system performance presents a BER floor. The accuracy of all the analysis carried out previously is verified in the next section.

B. MEAN CELLULAR SPECTRAL EFFICIENCY

In this subsection, an expression to calculate the mean cellular spectral efficiency, $\overline{\xi}$, is presented. For this, it is assumed the system does not operate when it is not able to guarantee a target BER, $P_{b,\mathrm{T}}$, i.e., if $\overline{P_b} > P_{b,\mathrm{T}}$, the system is in outage.

The cellular spectral efficiency calculation is based on the coverage area that can be provided for each modulation [43]. The pseudocode used to calculate the coverage radius[7] for each modulation is presented in Algorithm 1, where $\mathcal{R}_b$ denotes bit rate, which according to the Nyquist theorem is $\mathcal{R}_b \leq B_\mathrm{s}\log_2 M$, where B_s is the subcarrier bandwidth.

In the algorithm initial stage, some parameters are set according to the sector region to be evaluated. The inputs are the target BER, $P_{b,\mathrm{T}}$, the UEs maximum transmission power, $P_{t,\mathrm{M}}$, the noise power spectral density, N_0, and the bandwidth and power increase factor due to the cyclic prefix employed by the OFDMA system, which is written as

$$\epsilon = 1 + \frac{L_p}{L}, \tag{36}$$

where L_p is the number of cyclic prefix samples and L is the total number of subcarriers in the OFDMA system. The algorithm also requires R_i and R_f, which are respectively equal to R_0 and R_s for the inner sector region, or respectively equal to R_s and R for the sector outer region. Additionally, m is set to the highest order modulation (in the Algorithm 1: $M_1 > M_2 > M_3 > \ldots$). Furthermore, the value of δ_1 is an E_b/N_0 increment, δ_2 is an increment of the distance between a user and its serving BS, r, that is given in meters and ℓ is an auxiliary variable.

Algorithm 1 Coverage Radius Calculation for Each Modulation

Input: $P_{b,\mathrm{T}}, P_{t,\mathrm{M}}, N_0, \epsilon, R_\mathrm{i}, R_\mathrm{f}, \delta_1, \delta_2$

$r = R_\mathrm{i}$
for $m = M_1, M_2, M_3, \ldots$ **do**
  Obtain Δ as a function of E_b/N_0 employing (29)
  $\overline{P_b} = P_{b,\mathrm{T}}$, $E_b/N_0 = 0$, $\ell = 0$
  while $\overline{P_b} \geq P_{b,\mathrm{T}}$ **or** $\overline{P_b} - \ell \neq 0$ **do**
    $\ell = \overline{P_b}$
    Evaluate (33) with the current value of E_b/N_0
    $E_b/N_0 = E_b/N_0 + \delta_1$
  end while
  if $\overline{P_b} \leq P_{b,\mathrm{T}}$ **then**
    $P_r = N_0 \mathcal{R}_b E_b/N_0$, $P_t = 0$
    while $r \leq R_\mathrm{f}$ **or** $P_t \leq P_{t,\mathrm{M}}$ **do**
      $r = r + \delta_2$, $P_t = \epsilon P_r r^\beta$
    end while
  end if
  $\mathcal{R}_m = r$
end for

Output: $\mathcal{R}_{M_1}, \mathcal{R}_{M_2}, \mathcal{R}_{M_3}, \ldots$

[7]The coverage radius is the maximum distance from the BS that a target BER can be guaranteed for a certain modulation.

The algorithm first calculates Δ, given by (29), which is a function of E_b/N_0 (step 3). Then, E_b/N_0 is obtained recursively from (33) (steps 5 to 9). As previously said, the BER presents floors that cannot eliminated by increasing E_b/N_0. Thus, if $P_{b,\mathrm{T}}$ is not reached, or if a floor is detected, a lower order modulation is used. These aspects are validated in lines 5 and 10 of the algorithm. If all modulations have not been used yet, the modulation order is decreased and a new E_b/N_0 is obtained for this modulation. If $P_{b,\mathrm{T}}$ is reached, the received power at the BS is obtained in step 11. In order to determine the coverage radius for the current modulation, r is varied from R_i to R_f with δ_2 increments. The power transmitted by a UE is calculated in step 13, where the factor r^β appears due to the power control. If for a given r, $P_t \geq P_{t,\mathrm{M}}$, that value of r is the coverage radius for the current modulation, i.e., $\mathcal{R}_m = r$. Thus, $\mathcal{R}_m$ is the coverage radius for the modulation of order $m \in \{M_1, M_2, M_3, \ldots\}$. If all modulations have been used or if $r \geq R_\mathrm{f}$, the algorithm ends. The outputs are the coverage radii for all modulations. For a better understanding, consider Fig. 12, where $\mathcal{R}_{\mathrm{i},M_\ell}$ and $\mathcal{R}_{\mathrm{o},M_\ell}$ are the cell coverage radii with modulation M_ℓ for the inner and outer regions, respectively.

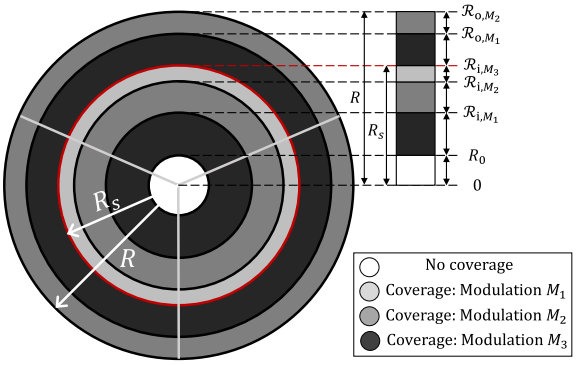

FIGURE 12. Cell coverage radii of the modulation schemes.

The computational complexity of Algorithm 1 depends on $P_{b,\mathrm{T}}$, δ_1, δ_2, and the number of modulations. However, this is not a real time algorithm, consequently, its execution time does not affect the system performance.

In the mean cellular spectral efficiency calculation, we assume that all cell sectors are affected by the same levels of CCI. In this case, $\overline{\xi}$ can be defined by the ratio between the total mean bit rate per cell and the total system bandwidth. Hence, for the SFR scenario we have that

$$\overline{\xi} = \frac{\overline{\mathcal{R}_{b,\mathrm{i}}} + \overline{\mathcal{R}_{b,\mathrm{o}}}}{\epsilon B}, \tag{37}$$

where B is the bandwidth for data transmission. As a consequence of the cyclic prefix, the total system bandwidth is ϵB, where ϵ is defined in (36). Besides, $\overline{\mathcal{R}_{b,\mathrm{i}}}$ and $\overline{\mathcal{R}_{b,\mathrm{o}}}$ are the mean bit rate of inner and outer cell regions, respectively. From the Nyquist theorem and by the random positioning of the users, these mean bit rates are respectively given by

$$\overline{\mathcal{R}_{b,\mathrm{i}}} = \mathcal{U}_\mathrm{i} \int_{R_0}^{R_s} B_\mathrm{s} \log_2 M(r) f\,(r; R_0, R_s)\, dr, \tag{38}$$

and

$$\overline{\mathcal{R}_{b,\mathrm{o}}} = \mathcal{U}_\mathrm{o} \int_{R_s}^{R} B_\mathrm{s} \log_2 M(r) f\,(r; R_s, R)\, dr, \tag{39}$$

where $\mathcal{U}_\mathrm{i}$ and $\mathcal{U}_\mathrm{o}$ denote the total number of users of the inner and outer regions of each cell, respectively. Further, $M(r)$ is the modulation order as a function of the distance between the UE and its BS, and the PDF $f\,(r; R_\mathrm{i}, R_\mathrm{f})$ is given by (2).

As users are uniformly distributed in the cell area, the number of users in each cell region is proportional to its area. Besides, we consider that all OFDMA subcarriers are used, i.e., $L = \mathcal{U}_\mathrm{i} + \mathcal{U}_\mathrm{o}$ and that $B = LB_\mathrm{s}$. Moreover, for a cellular system employing $\mathcal{M}$ modulations, the integrals of (38), and (39) can be separated as the sum of $\mathcal{M}$ integrals, where their integration limits are given by the coverage radius of each modulation. Hence, from (2), (38), and (39) and the above considerations, the mean cellular spectral efficiency of (37) can be rewritten as

$$\overline{\xi} = \frac{1}{\epsilon(R^2 - R_0^2)G} \left[\sum_{\ell=0}^{\mathcal{M}-1} \left(\mathcal{R}_{\mathrm{i},M_{\ell+1}}^2 - \mathcal{R}_{\mathrm{i},M_\ell}^2 \right) \log_2 M_{\ell+1} + \sum_{\ell=0}^{\mathcal{M}-1} \left(\mathcal{R}_{\mathrm{o},M_{\ell+1}}^2 - \mathcal{R}_{\mathrm{o},M_\ell}^2 \right) \log_2 M_{\ell+1} \right], \tag{40}$$

where $\mathcal{R}_{\mathrm{i},\mathcal{M}_0} = R_0$ and $\mathcal{R}_{\mathrm{o},\mathcal{M}_0} = R_s$. The factor $1/G$ appears because users transmit the same symbol on G radio channels in order to obtain diversity.

VI. NUMERICAL RESULTS AND DISCUSSIONS

In this section, the system performance is evaluated via numerical results. For this purpose, unless otherwise stated, it is considered that $R_0 = 20$ m, $R = 1000$ m, $\mathcal{H} = 1/3$, $\beta = 4$ and $2\sigma^2 = 1$, that is, the mean power of the non-line-of-sight (NLOS) multipaths has been normalized. In addition, the vector $\boldsymbol{\mathcal{K}} = [\mathcal{K}_1, \mathcal{K}_2, \ldots, \mathcal{K}_G]$ represents the Rice shape parameters for the G diversity branches.

A. MEAN BIT ERROR RATE

The mean BER is evaluated in this section employing the derived expressions in some representative scenarios. Monte Carlo simulations verify their accuracy.

Fig. 13 shows the mean BER as a function of E_b/N_0 for both inner and outer regions of the sector of interest, parameterized by $\boldsymbol{\mathcal{K}}$ and using the antenna radiation pattern $\mathcal{A}$, 16-QAM and $\mathcal{P}_c = 1$. In particular, $\boldsymbol{\mathcal{K}} = [5]$, $\boldsymbol{\mathcal{K}} = [5, 7]$ and $\boldsymbol{\mathcal{K}} = [5, 7, 9]$ imply $G = 1, 2$ and 3 branches, respectively. The vectors $\boldsymbol{\mathcal{K}}$ were chosen arbitrarily. Notice the accuracy of the exact BER expression with the simulation results and that the upper-bound is quite close to the exact BER. Observe also that as the diversity order increases, the CCI effects are mitigated and therefore, the BER decreases. However,

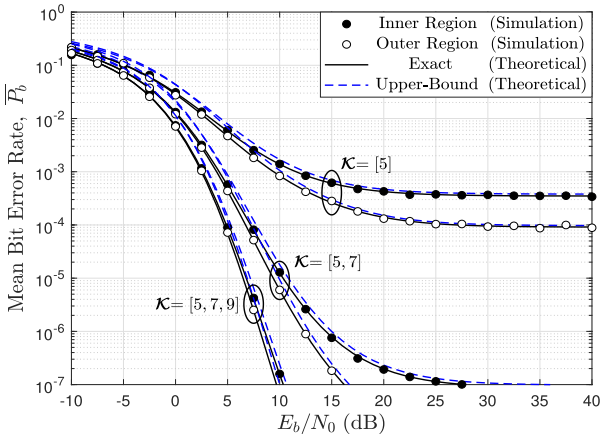

FIGURE 13. BER as a function of E_b/N_0 for both regions of the sector of interest, parameterized by $\mathcal{K}$ and considering the antenna radiation pattern $\mathcal{A}$, 16-QAM and $\mathcal{P}_c = 1$ in scenarios with $G = 1, 2$ and 3.

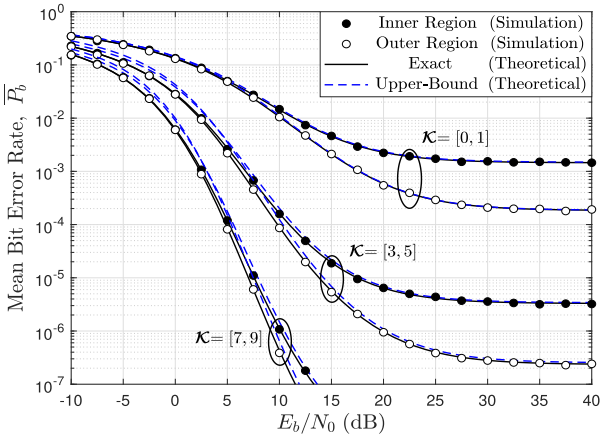

FIGURE 14. BER as a function of E_b/N_0 for both regions of the sector of interest, parameterized by $\mathcal{K}$ and considering the antenna radiation pattern $\mathcal{A}$, 16-QAM and $\mathcal{P}_c = 1$ in scenarios with $G = 2$.

as indicated at the end of Section V, there are floors in the BER curves, which are caused by the CCI. These floors appear at higher BER for the inner region. For the sector of interest outer region, the interferers are located only at the inner region of the co-cells. Thus, as these interferers are close to their BS, they transmit with low power. On the other hand, for the sector of interest inner region, some interferers are in the inner region of some co-cells, but other interferers are in the outer regions. Hence, these interferers use high transmission power, once they are further away from their BS. This produces a high CCI variance.

The next figure is similar to the previous one, once the same parameters are considered, except that Fig. 14 shows only scenarios with $G = 2$. In this figure, we can observe the impact that the values of $\mathcal{K}_g$ have on the system performance. When the power of the LOS component increases, the CCI effects are reduced. For this reason, the scenario with $\mathcal{K} = [7, 9]$ presents the best performance. As example, compare the BER curves for $\mathcal{K} = [5]$ in Fig. 13 with the curves for $\mathcal{K} = [0, 1]$ in Fig. 14. Notice that the first scenario, despite having diversity order 1 (or no diversity), presents better performance than the second scenario, where the diversity order is 2. This is due to the high ratio of the LOS path power to the NLOS multipaths power of the first scenario. This can be evidenced in (33), where although the diversity order G influences on the system performance, it is also important that the sum of the $\mathcal{K}_g$ factors is a high value to ensure a lower BER. Finally, observe that the derived BER upper-bound is more accurate when this sum of $\mathcal{K}_g$ factors is small. Despite that, the upper-bound is quite accurate for all scenarios.

Fig. 15 shows the mean BER as a function of E_b/N_0 for both regions of the sector of interest, parameterized by the modulation order (4-QAM, 64-QAM and 256-QAM) and considering the antenna pattern $\mathcal{A}$, $\mathcal{K} = [3, 5, 7]$, i.e., $G = 3$, and $\mathcal{P}_c = 1$. As expected, as the modulation order increases, the BER also increases for the same E_b/N_0. Thus, a higher modulation is more susceptible to the effects of CCI. However, based on previous results, if the LOS component power

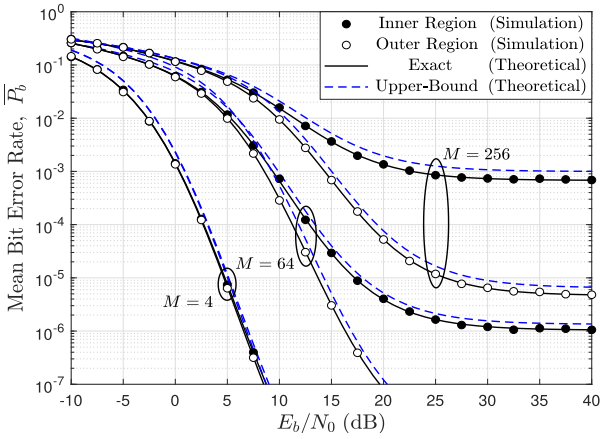

FIGURE 15. BER as a function of E_b/N_0 for both regions of the sector of interest, parameterized by the modulation order and considering the antenna radiation pattern $\mathcal{A}$, $\mathcal{K} = [3, 5, 7]$ and $\mathcal{P}_c = 1$.

is high, then acceptable BER can be achieved for a given telecommunication application. This figure also evidences that the derived upper-bound is more accurate for low order modulations. Nevertheless, it is still tight for evaluating the BER of high order modulations, like 256-QAM.

Fig. 16 shows the BER as a function of $\mathcal{P}_c$ for both inner and outer regions of the sector of interest, parameterized by the antenna radiation pattern, for $E_b/N_0 = 30$ dB, 64-QAM and $\mathcal{K} = [2, 4, 6, 8]$, that is, the diversity order is 4. In particular, the analytical radiation patterns of Fig. 4 and Fig. 5 were considered. From (16), it is known that the CCI variance is proportional to $\mathcal{P}_c$. Hence, in Fig. 16, note that as $\mathcal{P}_c$ increases, the mean BER also increases. By comparing the results of both antennas, note that the BER of antenna $\mathcal{A}$ is lower than that of antenna $\mathcal{U}$ for both cell regions. More specifically, the first antenna greatly attenuates signals outside the sector of interest, but the second antenna does not significantly attenuate undesirable signals from regions outside the angle interval $[-\pi/3, \pi/3]$. Obviously, the cost

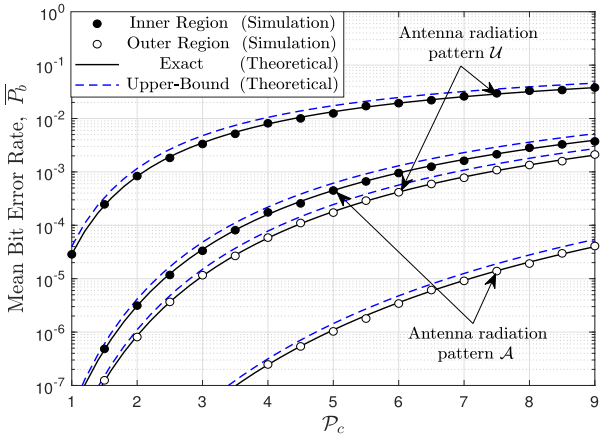

FIGURE 16. BER as a function of $\mathcal{P}_c$ for both regions of the sector of interest, parameterized by the antenna radiation pattern and considering $E_b/N_0 = 30$ dB, 64-QAM and $\mathcal{K} = [2, 4, 6, 8]$.

of reducing CCI is related to a smaller coverage area, since a more directive antenna is used. Consequently, one antenna mitigates CCI better than another, but at the cost of coverage.

Fig. 17 shows the mean BER as a function of the path-loss exponent, β, for both regions of the sector of interest, parameterized by the approach used to model non-ideal sectorization and by considering $E_b/N_0 = 30$ dB, 64-QAM, $\mathcal{K} = [1, 3, 5, 7, 9]$, i.e., $G = 5$, and $\mathcal{P}_c = 3$. The proposals of [38]–[40] were considered together with our proposal (antenna pattern $\mathcal{U}$). Thus, the non-ideal sectorization approaches of Fig. 3 and Fig. 4 are used. From (11), a higher β value means that the received power decays faster with the distance r. Therefore, as β increases, the BER decreases because the CCI power decreases. In the approach of [39], as v increases, more CCI is captured by the antenna and the BER increases. In this case, the BER of the inner region is greater than that of our proposal for both values of v. This is due to the CCI from the outer region of co-cell 3 (refer to Fig. 2) is not attenuated when non-ideal sectorization is modeled

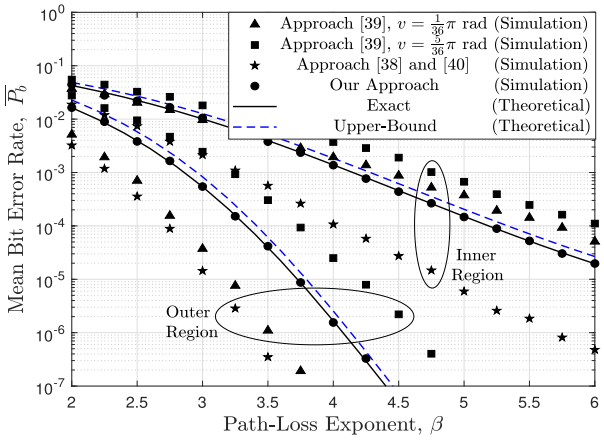

FIGURE 17. BER as a function of β for both regions of the sector of interest, parameterized by the approach to model non-ideal sectorization and considering $E_b/N_0 = 30$ dB, 64-QAM, $\mathcal{K} = [1, 3, 5, 7, 9]$ and $\mathcal{P}_c = 3$.

by a directive antenna having an additional opening angle that adds to the angle at which the sector is defined. In fact, CCI from the outer region of co-cell 3 is high because the interferer is far away from its serving BS and consequently, must transmit with high power. On the other hand, the outer region BER obtained with the proposal of [39] for $v = \pi/36$ rad is smaller than that obtained with our proposal. This is because the additional opening angle excludes all interference from co-cells 3 to 6. For $v = 5\pi/36$ rad, the mean BER increases because the CCI from co-cells 3 and 6 is also included. As this CCI is not attenuated, the BER is higher than that of our proposal. Finally, the approach used in [38] and [40] yields the lowest BER for both cell regions. This is due to the backside lobe used in this approach, that greatly attenuates the interference from co-cells 4 and 5. In addition, unlike the proposal of [39], in which interference from co-cells 3 and 6 is not attenuated as v increases, the radiation pattern presented in [38] greatly attenuates this interference and for this reason, it yields to a lower BER. Thus, in some cases, other proposals presented in the literature yield overly optimistic or pessimistic BER results, but we would like to clarify that our proposal is the most similar to real antenna radiation patterns.

All the previous scenarios consider $\mathcal{H} = 1/3$, that is, the cell outer region area is one-third of the total cell area. However, in order to observe the effects of the reuse radius, R_s, on the performance, we now consider some scenarios where $\mathcal{H}$ is different for each co-cell. In this paper, we focus on a target user performance by considering that there is always an interferer in each co-cell. Hence, this scenario is maintained in the following analysis despite that channel allocation within cells regions may change since R_s is modified. Thus, this is the worst case scenario.

By the above, Fig. 18 shows the BER as a function of E_b/N_0 for both regions of a sector, parameterized by the scenarios of Table 8 and considering the antenna radiation pattern $\mathcal{U}$, $\mathcal{K} = [3, 5, 7]$ and $\mathcal{P}_c = 2$. In this table, for $\mathcal{H}_j = 1/2$, $\mathcal{H}_j = 1/3$ and $\mathcal{H}_j = 1/4$, from (1) the ratio R_s/R is 0.707, 0.816 and 0.866, respectively. Based on the BER curves, the first scenario presents the worst performance, while the third scenario ensures the best performance for both sector regions. In this scenario, the inner region area of even co-cells is reduced. For both cell regions, there are less CCI levels from these co-cells, when compared to scenario 1, since interferers are close to their BSs and consequently,

TABLE 8. $\mathcal{H}$ for the j-th co-cell for each scenario presented in Fig. 18.

$\mathcal{H}_j$	Scenario 1	Scenario 2	Scenario 3	Scenario 4
$\mathcal{H}_1$	1/3	1/2	1/3	1/3
$\mathcal{H}_2$	1/3	1/3	1/2	1/4
$\mathcal{H}_3$	1/3	1/2	1/3	1/2
$\mathcal{H}_4$	1/3	1/3	1/2	1/3
$\mathcal{H}_5$	1/3	1/2	1/3	1/2
$\mathcal{H}_6$	1/3	1/3	1/2	1/2

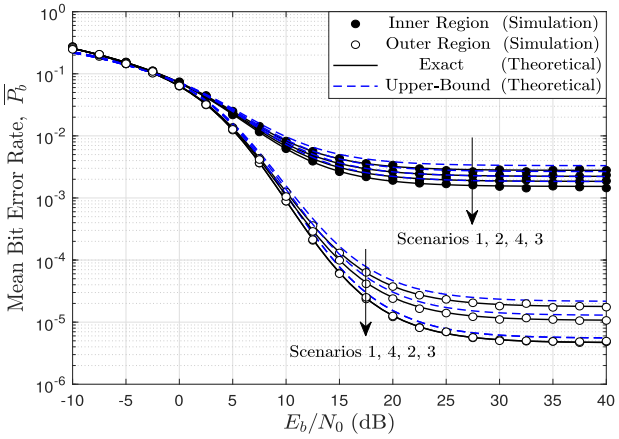

FIGURE 18. BER as a function of E_b/N_0 for both regions of the sector of interest, parameterized by the scenarios of Table 8 and considering the antenna radiation pattern $\mathcal{U}$, $\mathcal{K} = [3, 5, 7]$ and $\mathcal{P}_c = 2$.

they employ low transmission powers. The second scenario is superior to the first scenario but inferior to the third one for the inner region. In this case, the inner region area of odd co-cells is reduced, consequently, the outer region area of these co-cells is increased. The CCI affecting the sector of interest inner region is reduced because interferers in outer regions of odd co-cells may be closer to their service BS, therefore, on average, they use lower power levels when compared to scenario 1. However, the CCI reduction, and consequently, the BER improvement is not as great as in scenario 3 because interferers in outer regions always transmit with higher power than those in inner regions. On the other hand, due to hexagonal symmetry, the sector of interest outer region in scenario 2 has exactly the same performance as the outer region in scenario 3. Scenario 4 considers arbitrary values of $\mathcal{H}$ for the co-cells. This scenario and the previous ones show that the derived expressions are quite accurate with the simulation results. In particular, the fourth scenario presents the second best performance for the inner region and the third best performance for the outer region. Finally, notice that modifying R_s in the co-cells affects to a greater extent the performance of the users in the outer region. In fact, this happens because these users are the most susceptible to CCI.

B. MEAN CELLULAR SPECTRAL EFFICIENCY

The mean cellular spectral efficiency is evaluated in this subsection employing Algorithm 1 and (40). For this, we use some parameters of the LTE standard [52]. An OFDMA system is evaluated with $L = 1200$ subcarriers, each with $B_s = 15$ kHz, $L_p = 95$ samples, $P_{t,M} = 23$ dBm, and $N_0 = -174$ dBm/Hz. We also assume that the Rician $\mathcal{K}$ factor may change as UE moves away from their serving BS. Thus, the shorter the distance between them, the greater $\mathcal{K}$ is. At the edge of the cell it is more likely that $\mathcal{K} = 0$, once there is NLOS between the BS and an UE.

By the above, we have established three intervals for the distance between an UE and the BS. If there is diversity of order G, then G Rician $\mathcal{K}$ factors are assigned to each interval. In our analysis, we have also assumed that $\mathcal{P}_c = 1$, that is, co-cell interferers have NLOS with the BS of interest. Moreover, as $R_0 = 20$ m, $R = 1000$ m and $\mathcal{H} = 1/3$, then $R_s = 816.6$ m. In addition, the 3 different scenarios shown in Table 9 are considered. Notice that scenarios X, Y and Z employ $G = 2$, $G = 3$ and $G = 4$, respectively. Finally, it is considered that the cellular system employs 4-QAM, 16-QAM and 64-QAM.

Fig. 19 shows the normalized coverage radius for each modulation used in the system as a function of the target BER, $P_{b,\mathrm{T}}$, parameterized by the scenarios shown in Table 9. These results are obtained employing the Algorithm 1. Observe that for $P_{b,\mathrm{T}} = 10^{-3}$, the system uses 16-QAM and 64-QAM throughout the cell. As example, in scenario Z, the system uses 64-QAM in almost all inner cell region and in all outer region. Without sectorization and SFR, this would not be possible due to high CCI levels. On the other hand, as $P_{b,\mathrm{T}}$ is reduced, the cellular system must employ lower order modulations in order to ensure the target BER for all UEs. Notice that the cellular system cannot ensure $P_{b,\mathrm{T}} = 10^{-6}$ in the outer cell region for scenario X. This occurs because this scenario presents the lowest diversity order ($G = 2$) and therefore has less immunity to fading and interference. In addition, observe that for $P_{b,\mathrm{T}}$ of 10^{-5} or 10^{-6}, UEs cannot employ 64-QAM in any cell region.

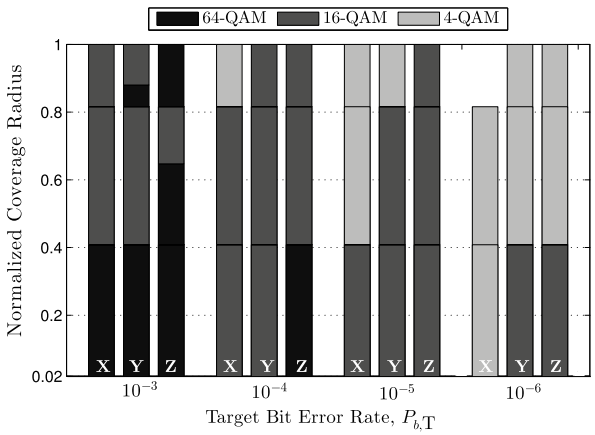

FIGURE 19. Normalized coverage radius for each modulation as a function of $P_{b,\mathrm{T}}$ for scenarios of Table 9.

TABLE 9. Rician $\mathcal{K}$ factors as a function of the distance between UEs and their BS, r, for three different scenarios.

r Interval	Scenario X	Scenario Y	Scenario Z
$R_0 \le r < R_s/2$	$\mathcal{K} = [6, 7]$	$\mathcal{K} = [4, 6, 7]$	$\mathcal{K} = [3, 3, 6, 7]$
$R_s/2 \le r < R_s$	$\mathcal{K} = [4, 6]$	$\mathcal{K} = [1, 4, 5]$	$\mathcal{K} = [1, 2, 3, 4]$
$R_s \le r \le R$	$\mathcal{K} = [1, 2]$	$\mathcal{K} = [0, 1, 2]$	$\mathcal{K} = [0, 1, 1, 1]$

Fig. 20 shows the mean spectral efficiency obtained for the scenarios of Table 9, which is calculated using the coverage radii of Fig. 19 and (40). As the $P_{b,\mathrm{T}}$ is reduced,

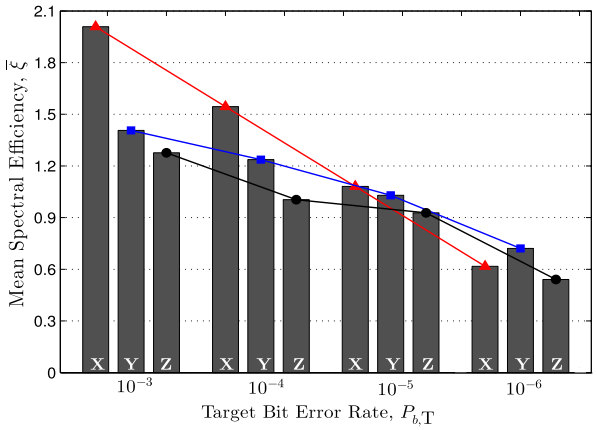

FIGURE 20. Mean cellular spectral efficiency as a function of $P_{b,\mathrm{T}}$ for scenarios of Table 9.

$\overline{\xi}$ decreases because UEs must use lower order modulations. For $P_{b,\mathrm{T}} = 10^{-3}, 10^{-4}$ and 10^{-5}, scenario X presents the best spectral efficiency because the lowest diversity order is employed and despite this, the target BER is guaranteed. In this work, frequency or time diversity are assumed, which represent loss in spectral efficiency at a cost of improving the system performance. On the other hand, notice that for $P_{b,\mathrm{T}} = 10^{-6}$, the scenario Y presents the best spectral efficiency. In this case, scenario X no longer guarantees the target BER in the outer cell region and therefore, it does not have the best spectral efficiency. Moreover, note in Fig. 19 that for this value of $P_{b,\mathrm{T}} = 10^{-6}$, the Y and Z scenarios use the same modulations. However, scenario Y has better spectral efficiency because it uses a lower diversity order. By the above, the algorithm and the proposed expressions can be used to determine scenarios that maximize the system spectral efficiency under different configurations.

VII. CONCLUSIONS

The performance of non-ideal sectorized OFDMA cellular systems was analyzed assuming that SFR and power control are used to reduce CCI levels. Non-ideal sectorization was emulated taking as a reference the radiation pattern of real antennas. The channel assumed path-loss and Rician fading. In order to counteract the fading effects, a MRC stage was used in the receiver at the BS. The fading affecting the signals of the diversity branches are characterized because they have different Rician $\mathcal{K}$ factors, this is, unbalanced diversity.

The analysis showed that the CCI received in each branch can be modeled as a zero-mean Gaussian random variable whose variance depends mainly on the cell region a target user is located. An exact expression to calculate the CCI variance was derived. From this analysis, we observed for the SFR scenario, that outer region users are less affected by CCI than inner region users when the same Rician $\mathcal{K}$ factors are assumed in the fading channel. An exact single-integral expression to calculate the mean BER of a target user was derived. Then, a closed-form upper-bound expression was obtained, which is tight to the exact BER in all the SNR regimes and even for high order modulations. Unlike expressions of [13], where first is necessary to determine some parameters related to the constellation decision boundaries, our expressions can be used directly for any square M-QAM.

An algorithm that calculates the coverage radius for each modulation of the analyzed system was presented. which can be used for dimensioning or/and analyzing cellular systems, as long as BER expressions are available. Its computational complexity may vary from scenario to scenario. However, as it is an analytical tool, its execution time is not related to the system performance. In addition, an expression that evaluates the cellular spectral efficiency was obtained, which allows to analyze scenarios that maximize $\overline{\xi}$ and guarantee a target BER in both cell regions. From the results, it was observed that the number of diversity branches, the sum of the $\mathcal{K}$ factors of these branches, and the antenna type are decisive to guarantee the target BER and to maximize $\overline{\xi}$.

Two commercial antennas were used as reference to emulate imperfect sectorization. However, in practice, any antenna can be chosen based on network planning. In fact, our proposal allows any directive antenna to be used in the proposed system model. We compared our imperfect sectorization approach with other proposals in the literature. Results showed that other proposals may be too optimistic or pessimistic because they do not resemble the radiation pattern of a real antenna. Although the analysis was made considering cells divided into three sectors, it can be easily modified for scenarios with more than three sectors.

For the proposal presented in this work, it is necessary to know the Rician $\mathcal{K}$ factor for each diversity branch, which is a problem of channel estimation. However, some recent techniques have been proposed to estimate these factors in different scenarios [53]–[56]. Finally, aspects such as imperfect CSI and correlated fading between diversity branches were not considered in our proposal. Hence, they are interesting extensions for future investigation. Besides, as non-ideal sectorization using SFR was analyzed for the first time, a cellular scheme based on hexagonal and circular geometries was used as a first approach in this paper. Thus, non-ideal sectorization of random cellular networks based on Voronoi tessellation [57] is also an interesting option for future work.

APPENDIX
UPPER-BOUND FOR THE INTEGRAL $\mathcal{I}$

An upper-bound of the integral $\mathcal{I}$, defined in (31), is obtained in this appendix.

From (28), (30) and (31), $\mathcal{I}$ is rewritten as

$$\mathcal{I} = \frac{1}{\pi}\int_0^{\pi/2} f(x)dx, \tag{41}$$

where $f(x) = f_1(x)f_2(x)$, and $f_1(x)$ and $f_2(x)$ are defined respectively as

$$f_1(x) = \left[\frac{\sin^2(x)}{\sin^2(x) + m_\kappa}\right]^G, \tag{42}$$

$$f_2(x) = \prod_{g=1}^{G} \exp\left(-\frac{\Gamma \nu_\kappa \mu_g^2}{\sin^2(x) + 2\sigma^2 \Gamma \nu_\kappa}\right) = \exp\left(-\frac{m_\kappa}{\sin^2(x) + m_\kappa} \sum_{g=1}^{G} \mathcal{K}_g\right), \quad (43)$$

where we have used (9) and m_κ is defined in (34)

The primitive of $\int_0^{\pi/2} f_1(x)dx$ can be found. Hence, in order to obtain an approximation of (41), Taylor series expansion [51, Eq. (0.318.1)] is used on $f_2(x)$. Consequently,

$$\mathcal{I} = \frac{1}{\pi} \int_0^{\pi/2} f_1(x) \sum_{n=0}^{\infty} \frac{(x - x_0)^n}{n!} f_2^{(n)}(x_0) dx, \quad (44)$$

where $f^{(n)}(x_0)$ is the n-th derivative of $f(x)$ evaluated at x_0. The derivative of order zero of $f(x)$ is $f(x)$ itself. The integrals of the terms for $n > 0$ do not have closed-form. Thus, as our goal is to find a closed-form approximation, we will use only the first term of the expansion.

Due to the single-term Taylor series expansion, the point x_0 takes an important role in the approximation. In general, the idea of this series expansion is to evaluate $f(x)$, when x is very close to x_0. This means that the closer x is to x_0, less terms are used to obtain a reliable precision. However, we are interested in evaluating an integral for $0 \leq x \leq \pi/2$. Therefore, the selection of x_0 must follow another criterion. In particular, we are interested in the worst-case performance of a telecommunication system. Thus, an accurate upper-bound performance indicator is an interesting tool. In this sense, the selection of x_0 is motivated by this aspect.

By the above, $f(x)$ can be approximated by

$$\tilde{f}(x, x_0) \approx \left[\frac{\sin^2(x)}{\sin^2(x) + m_\kappa}\right]^G \exp\left(-\frac{m_\kappa}{\sin^2(x_0) + m_\kappa} \sum_{g=1}^{G} \mathcal{K}_g\right). \quad (45)$$

As example, we have chosen two scenarios to show the behavior of $f(x)$ and its approximation. They are shown in Fig. 21 as a function of x. The approximations are plotted for different values of x_0. Fig. 21a considers $m_\kappa = 4.5$ and[8] $\mathcal{K} = [2, 4]$. On the other hand, Fig. 21b uses $m_\kappa = 3$ and $\mathcal{K} = [0, 1, 3, 5]$. In the figure, note the exact function and the approximations intersect at x_0. Thus, we could find an appropriate x_0 value from $\int_0^{x_0} [\tilde{f}(x, x_0) - f(x)]dx = \int_{x_0}^{\pi/2} [f(x) - \tilde{f}(x, x_0)]dx$, but, this involves the numerical resolution of the exact integral, which we want to avoid.

From another point of view, Fig. 21 shows that a Taylor expansion around $x_0 = 0$ (Maclaurin series [51, Eq. (0.318.2)]) generates a lower-bound for the integral calculation. In fact, it may not be precise enough because the area under the approximate curve is much smaller than that under the exact curve. In contrast, notice that values of x_0 close to $\pi/2$ approximate the area under the curve in a better way. However, depending on the values of $\mathcal{K}_g$ and m_κ, a same

[8]We have used the notation $\mathcal{K} = [\mathcal{K}_1, \mathcal{K}_2, \ldots, \mathcal{K}_G]$

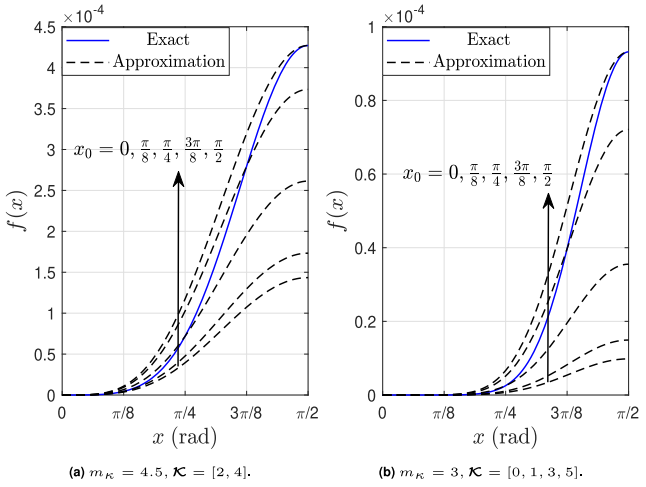

(a) $m_\kappa = 4.5, \mathcal{K} = [2, 4]$. (b) $m_\kappa = 3, \mathcal{K} = [0, 1, 3, 5]$.

FIGURE 21. Approximations for the function $f(x)$ parameterized by x_0 considering two different scenarios.

value of x_0 can generate a lower-bound or an upper-bound for the integral. For example, for the scenario of Fig. 21a, the exact value of $\mathcal{I}$ is 2.236×10^{-3} and the approximate value with $x_0 = 3\pi/8$ is 2.271×10^{-3}. In Fig. 21b, the exact value of the integral is 3.489×10^{-4} and the approximate value of $\mathcal{I}$ with the same value of x_0 is 3.179×10^{-4}. Hence, having an expression that behaves sometimes as a lower-bound and sometimes as an upper-bound is not desirable.

From the previous results, we realize that using $x_0 = \pi/2$ rad always guarantee an upper-bound for the integral value. Hence, considering $x_0 = \pi/2$ rad, the upper-bound for $\mathcal{I}$ can be calculated as

$$\mathcal{I} \leq \exp\left(-\frac{m_\kappa}{1 + m_\kappa} \sum_{g=1}^{G} \mathcal{K}_g\right) \underbrace{\frac{1}{\pi} \int_0^{\pi/2} \left[\frac{\sin^2(x)}{\sin^2(x) + m_\kappa}\right]^G dx}_{\mathcal{L}}. \quad (46)$$

Therefore, from [50, Sections 9.2.2 and 9.2.3], it is possible to realize that $\mathcal{L}$ has a closed-form expression given by

$$\mathcal{L} = \left(\frac{1 - \rho_\kappa}{2}\right)^G \sum_{j=0}^{G-1} \binom{G - 1 + j}{j} \left(\frac{1 + \rho_\kappa}{2}\right)^j, \quad (47)$$

where ρ_κ is defined by (35). Finally, notice that if $\mathcal{K}_g = 0, \forall g$, $\mathcal{I}$ is similar to the well known expression to evaluate the BER of MRC with BPSK modulation in Rayleigh fading channels [8, Eq. (14-4-15)].

REFERENCES

[1] N. Al-Falahy and O. Y. Alani, "Technologies for 5G networks: Challenges and opportunities," *IT Prof.*, vol. 19, no. 1, pp. 12–20, Jan. 2017.
[2] 5G Americas, "New services and applications with 5G ultra-reliable low latency communications," 5G Americas, Bellevue, WA, USA, White Paper, Nov. 2018. [Online]. Available: https://www.5gamericas.org/new-services-applications-with-5g-ultra-reliable-low-latency-communications/
[3] A. Abdi, C. Tepedelenlioglu, M. Kaveh, and G. Giannakis, "On the estimation of the k parameter for the rice fading distribution," *IEEE Commun. Lett.*, vol. 5, no. 3, pp. 92–94, Mar. 2001.

[4] K. Jiang, Z. Liu, P. Yang, Y. Xiao, and S. Li, "An experimental investigation of enhanced SM-OFDM over indoor rician multipath channels," *IEEE Trans. Veh. Technol.*, vol. 69, no. 2, pp. 2291–2295, Feb. 2020.

[5] Z. Du, J. Cheng, and N. C. Beaulieu, "BER analysis of BPSK signals in ricean-faded cochannel interference," *IEEE Trans. Commun.*, vol. 55, no. 10, pp. 1994–2001, Oct. 2007.

[6] P. Cardieri and T. S. Rappaport, "Statistical analysis of co-channel interference in wireless communications systems," *Wireless Commun. Mobile Comput.*, vol. 1, no. 1, pp. 111–121, Jan. 2001.

[7] M. Lopez-Benitez, "Outage probability and average error performance of modulation schemes under Nakagami-q (Hoyt) and Nakagami-n (Rice) fading channels," in *Proc. 10th Int. Symp. Commun. Syst., Netw. Digit. Signal Process. (CSNDSP)*, Jul. 2016, pp. 1–6.

[8] J. Proakis and D. Manolakis, *Digital Communications*, 4th ed. New York, NY, USA: McGraw, NY, 2007.

[9] S. Vasana and P. J. McLane, "Diagonalizer for correlated or unbalanced diversity branches in Rayleigh or rician fading channels and wireless communication," in *Proc. IEEE Electro/Inf. Technol. Conf.*, Aug. 2004, pp. 1–6.

[10] R. Valenzuela, L. Ahumada, and R. Feick, "The effect of unbalanced branches on the performance of diversity receivers for urban fixed wireless links," *IEEE Trans. Wireless Commun.*, vol. 6, no. 9, pp. 3324–3332, Sep. 2007.

[11] A. S. Panajotovic, N. M. Sekulovic, M. C. Stefanovic, and D. L. Draca, "Average level crossing rate of dual selection diversity over correlated unbalanced Nakagami-m fading channels in the presence of cochannel interference," *IEEE Commun. Lett.*, vol. 16, no. 5, pp. 691–693, May 2012.

[12] Y. Ma, "Impact of correlated diversity branches in rician fading channels," in *Proc. IEEE Int. Conf. Commun. ICC*, May 2005, pp. 473–477.

[13] Y. Ma, R. Schober, and D. Zhang, "Exact BER for M-QAM with MRC and imperfect channel estimation in rician fading channels," *IEEE Trans. Wireless Commun.*, vol. 6, no. 3, pp. 926–936, Mar. 2007.

[14] T. T. Ha, *Theory and Design of Digital Communication Systems*. New York, NY, USA: Cambridge Univ. Press, 2011.

[15] N. C. Beaulieu and S. Wei, "Complete solutions for the outage probability of maximal ratio combining diversity on Nakagami-m fading channels with unequal power branches valid for integer m," *IET Commun.*, vol. 13, no. 17, pp. 2714–2722, Oct. 2019.

[16] F. J. Lopez-Martinez, L. Moreno-Pozas, U. Fernandez-Plazaola, J. F. Paris, E. Martos-Naya, and J. M. Romero-Jerez, "A tractable Line-of-Sight product channel model: Application to wireless powered communications," in *Proc. 15th Int. Symp. Wireless Commun. Syst. (ISWCS)*, Aug. 2018, pp. 1–5.

[17] Z. Wu, K. Lu, C. Jiang, and X. Shao, "Comprehensive study and comparison on 5G NOMA schemes," *IEEE Access*, vol. 6, pp. 18511–18519, Mar. 2018.

[18] L. Dai, B. Wang, Z. Ding, Z. Wang, S. Chen, and L. Hanzo, "A survey of non-orthogonal multiple access for 5G," *IEEE Commun. Surveys Tuts.*, vol. 20, no. 3, pp. 2294–2323, 3rd Quart., 2018.

[19] P. Korrai, E. Lagunas, S. K. Sharma, S. Chatzinotas, A. Bandi, and B. Ottersten, "A RAN resource slicing mechanism for multiplexing of eMBB and URLLC services in OFDMA based 5G wireless networks," *IEEE Access*, vol. 8, pp. 45674–45688, Mar. 2020.

[20] T. Rappaport, *Wireless Communications, Principles and Practice*. Upper Saddle River, NJ, USA: Prentice-Hall, 1996.

[21] Y.-W. Kuo, C. C. Lu, and G.-Y. Shen, "Adaptive resource allocation for downlink grouped MC-CDMA systems with power and BER constraints," *AEU Int. J. Electron. Commun.*, vol. 68, no. 1, pp. 25–32, Jan. 2014.

[22] C.-C. Josefina, M.-A. Gerardo, C. Liliana, G.-A.-J. E. Moisés, G.-C.-J. Fermi, and M.-H.-G. Ardul, "Montecarlo simulation applied to measurement of the impact of the smart antenna technology in digital cellular systems," *Ingeniería, Investigación y Tecnología*, vol. 16, no. 2, pp. 207–212, Apr. 2015.

[23] C. Gueguen, M. Ezzaouia, and M. Yassin, "Inter-cellular scheduler for 5G wireless networks," *Phys. Commun.*, vol. 18, pp. 113–124, Mar. 2016.

[24] R. Ghaffar and R. Knopp, "Fractional frequency reuse and interference suppression for OFDMA networks," in *Proc. 8th Int. Symp. Modeling Optim. Mobile, Ad Hoc, Wireless Netw.*, Avignon, France, May 2010, pp. 273–277.

[25] H. Holma, A. Toskala, and J. Reunanen, *LTE Small Cell Optimization: 3GPP Evolution to Release*. West Sussex, U.K.: Wiley, 2016.

[26] S. C. Lam, K. Sandrasegaran, and T. N. Quoc, "Performance of soft frequency reuse in random cellular networks in Rayleigh-lognormal fading channels," in *Proc. 22nd Asia–Pacific Conf. Commun. (APCC)*, Aug. 2016, pp. 481–487.

[27] I. I. Mahmoud, O. H. Elgzzar, S. Hashima, and H. A. Konber, "An accurate model of worst case signal to interference ratio for frequency reuse cellular systems," in *Proc. 11th Int. Conf. Comput. Eng. Syst. (ICCES)*, Dec. 2016, pp. 393–400.

[28] F. Hamdani, A. Maurizka, M. M. Ulfah, and Iskandar, "Power ratio evaluation for soft frequency reuse technique in LTE-A heterogeneous networks," in *Proc. 11th Int. Conf. Telecommun. Syst. Services Appl. (TSSA)*, Oct. 2017, pp. 1–5.

[29] N. Feng, S. Lin, G. Zhu, S. Li, and H. Zhang, "Interference performance analysis of frequency reuse techniques for LTE-R systems," in *Proc. 21st Int. Conf. Intell. Transp. Syst. (ITSC)*, Nov. 2018, pp. 3415–3420.

[30] A. Entezari and A. Tadaion, "Coverage and rate analysis in cellular networks with Nakagami-Lognormal fading channel employing soft frequency reuse," *Phys. Commun.*, vol. 36, pp. 1–7, Oct. 2019.

[31] J. Garcia-Morales, G. Femenias, and F. Riera-Palou, "Higher order sectorization in FFR-aided OFDMA cellular networks: Spectral- and energy-efficiency," *IEEE Access*, vol. 7, pp. 11127–11139, Jan. 2019.

[32] A. Adejo, S. Boussakta, and J. Neasham, "Interference modelling for soft frequency reuse in irregular heterogeneous cellular networks," in *Proc. 9th Int. Conf. Ubiquitous Future Netw. (ICUFN)*, Jul. 2017, pp. 381–386.

[33] M. S. Hossain, F. Tariq, and G. A. Safdar, "Enhancing cell-edge performance using multi-layer soft frequency reuse scheme," *Electron. Lett.*, vol. 51, no. 22, pp. 1826–1828, Oct. 2015.

[34] A. Boustani, N. Mirmotahhary, R. Danesfahani, and S. Khorsandi, "An efficient frequency reuse scheme by cell sectorization in OFDMA based wireless networks," in *Proc. 4th Int. Conf. Comput. Sci. Converg. Inf. Technol.*, Nov. 2009, pp. 800–805.

[35] F. Wamser, D. Mittelstadt, and D. Staehle, "Soft frequency reuse in the uplink of an OFDMA network," in *Proc. IEEE 71st Veh. Technol. Conf.*, Taipei, Taiwan, May 2010, pp. 1–5.

[36] I. Guío, Á. Hernández, J. Chóliz, and A. Valdovinos, "Resource allocation strategies for full frequency reuse in tri-sectorized multi-cell orthogonal frequency division multiple access systems," *Wireless Commun. Mobile Comput.*, vol. 14, no. 2, pp. 297–320, Feb. 2014.

[37] B. Malini and K. V. Babu, "Soft frequency reuse based interference minimization technique for long term evolution-advanced heterogeneous networks," in *Proc. Int. Conf. Commun. Signal Process. (ICCSP)*, Chennai, India, Apr. 2017, pp. 0630–0634.

[38] S.-W. Wang and I. Wang, "Effects of soft handoff, frequency reuse and non-ideal antenna sectorization on CDMA system capacity," in *Proc. IEEE 43rd Veh. Technol. Conf.*, May 1993, pp. 850–854.

[39] M. G. Jansen and R. Prasad, "Capacity, throughput, and delay analysis of a cellular DS CDMA system with imperfect power control and imperfect sectorization," *IEEE Trans. Veh. Technol.*, vol. 44, no. 1, pp. 67–75, Feb. 1995.

[40] J. Casta neda-Camacho, C. E. Uc-Rios, and D. Lara-Rodriguez, "Reverse Link Erlang Capacity of Multiclass CDMA Cellular System Considering Nonideal Antenna Sectorization," *IEEE Trans. Veh. Technol.*, vol. 52, no. 6, pp. 1476–1486, Nov. 2003.

[41] H. R. Carvajal Mora, N. V. Orozco Garzon, and C. de Almeida, "BER analysis of overloaded MC-CDMA cellular system employing sphere decoder in non-ideal sectorization scenario," in *Proc. IEEE 13th Int. Conf. Wireless Mobile Comput., Netw. Commun. (WiMob)*, Oct. 2017, pp. 1–8.

[42] Y. Chen, "Achieve high spectral efficiency for 5G: Multi-user MIMO versus NOMA," in *Proc. IEEE 89th Veh. Technol. Conf. (VTC-Spring)*, Apr. 2019, pp. 1–5.

[43] H. Carvajal, N. Orozco, and C. de Almeida, "Mean spectral efficiency evaluation of the uplink of MC-CDMA cellular systems," *Wireless Pers. Commun.*, vol. 96, no. 3, pp. 4595–4611, May 2017.

[44] A. Papoulis and S. Pillai, *Probability, Random Variables and Stochastic Processes*, 4th ed. New York, NY, USA: McGraw-Hill, 2002.

[45] M. Abramowitz and I. A. Stegun, "Handbook of mathematical functions with formulas, graphs and mathematical tables," Dept. Commerce, Dover, Washington, DC, USA, 1964.

[46] H. Holma and A. Toskala, *LTE for UMTS: Evolution to LTE-Advanced*. Hoboken, NJ, USA: Wiley, 2011.

[47] *LTE Evolved Universal Terrestrial Radio Access (E-UTRA): Physical Layer Procedures*, Standard 3GPP TS 36.213 version 13.2.0 Release 13, Tech. Rep., 2016.

[48] *LTE–E-UTRA: User Equipment (UE) Radio Transmission and Reception*, Standard 3GPP TS 36.101 vers. 14.3.0 Release 14, Tech. Rep., 2017.
[49] K. Cho and D. Yoon, "On the general BER expression of one- and two-dimensional amplitude modulations," *IEEE Trans. Commun.*, vol. 50, no. 7, pp. 1074–1080, Jul. 2002.
[50] M. K. Simon and M. Alouini, *Digital Communication over Fading Channels*. 2nd. ed. Hoboken, NJ, USA: Wiley, 2002.
[51] I. Gradshteyn, and I. Ryzhik, *Table of Integrals, Series, and Products*, 7th ed. Amsterdam, The Netherlands: Elsevier, 2007.
[52] H. Holma, and A. Toskala. LTE for UMTS, *Evolution to LTE-Advanced*, 2nd ed. West Sussex, U.K.: Wiley, 2011.
[53] P. Tang, J. Zhang, A. F. Molisch, P. J. Smith, M. Shafi, and L. Tian, "Estimation of the K-Factor for temporal fading from single-snapshot wideband measurements," *IEEE Trans. Veh. Technol.*, vol. 68, no. 1, pp. 49–63, Jan. 2019.
[54] W. Zhang, "Method of moment rice parameter estimators with improved performance at low SNR," in *Proc. 13th Int. Conf. Signal Process. Commun. Syst. (ICSPCS)*, Dec. 2019, pp. 1–5.
[55] X. Leturc, P. Ciblat, and C. J. Le Martret, "Estimation of the Ricean *K* factor in the presence of shadowing," *IEEE Commun. Lett.*, vol. 24, no. 1, pp. 108–112, Oct. 2019.
[56] J. Yu, W. Chen, F. Li, C. Li, K. Yang, Y. Liu, and F. Chang, "Channel measurement and modeling of the small-scale fading characteristics for urban inland river environment," *IEEE Trans. Wireless Commun.*, vol. 19, no. 5, pp. 3376–3389, May 2020.
[57] J. G. Andrews, F. Baccelli, and R. K. Ganti, "A tractable approach to coverage and rate in cellular networks," *IEEE Trans. Commun.*, vol. 59, no. 11, pp. 3122–3134, Nov. 2011.

HENRY CARVAJAL (Member, IEEE) received the B.Sc. degree in electronics and telecommunications engineering from Armed Forces University-ESPE, Ecuador, in 2009, and the M.Sc. and Ph.D. degrees in electrical engineering from the School of Electrical and Computer Engineering (FEEC), University of Campinas (UNICAMP), Brazil, in 2014 and 2018, respectively. He was ranked first in his undergraduate program. He was the Director of the Technology Transfer Area in the Education, Science, and Technology Secretariat (SENESCYT), Ecuador, in 2018. He is currently a Full Professor with the Universidad de Las Américas (UDLA), Quito, Ecuador. His research interests include fading channels, diversity-combining systems, orthogonal and non-orthogonal multiple access, multiuser detection, MIMO, 5G, and B5G technologies.

NATHALY OROZCO received the Electronic and Telecommunications Engineering degree from Armed Forces University-ESPE, Sangolquí, Ecuador, in 2011, and the M.Sc. and Ph.D. degrees in electrical engineering from the University of Campinas (UNICAMP), Brazil, in 2014 and 2018, respectively. She is currently a Full Professor with the Universidad de Las Américas (UDLA), Quito, Ecuador. Her research interests include digital communications with specific emphasis on orthogonal and non-orthogonal multiple access, fading channels, MIMO, cognitive systems, opportunistic transmissions, and 5G technologies.

DANIEL ALTAMIRANO (Student Member, IEEE) received the Electronic and Telecommunications Engineering degree from the Universidad de las Fuerzas Armadas-ESPE, Sangolquí, Ecuador, in 2008, and the M.Sc. degree in electrical engineering from the University of Campinas (UNICAMP), Brazil, in 2011, where he is currently pursuing the Ph.D. degree. He is a Full Professor with the Universidad de las Fuerzas Armadas-ESPE. His research interests include digital communications with specific emphasis on multiple access techniques, fading channels, MIMO, error control coding, software defined radio, and 5G technologies.

CELSO DE ALMEIDA received the Electrical Engineering, M.Sc., and Ph.D. degrees from the State University of Campinas (UNICAMP), Brazil, in 1980, 1983, and 1990, respectively. He joined the Electrical Engineering Faculty with UNICAMP, in 1990, where he is currently a Full Professor. He worked as an Electrical Engineer in the industry, from 1982 to 1990, with focus in optical communications. His research interest include digital communications, cellular systems, orthogonal and non-orthogonal multiple access, multiuser detection, antenna arrays, MIMO systems, wireless communications, cryptography, and error correction codes.